Advective Ocean–Atmosphere Interaction: An Analytical Stochastic Model with Implications for Decadal Variability

R. SARAVANAN

*National Center for Atmospheric Research, Boulder, Colorado**

JAMES C. MCWILLIAMS

Department of Atmospheric Sciences, University of California, Los Angeles, Los Angeles, California

(Manuscript received 8 January 1997, in final form 21 May 1997)

ABSTRACT

Atmospheric variability on timescales of a month or longer is dominated by a small number of large-scale spatial patterns (''teleconnections''), whose time evolution has a significant stochastic component because of weather excitation. One may expect these patterns to play an important role in ocean–atmosphere interaction. On interannual and longer timescales, horizontal advection in the ocean can also play an important role in such interaction. The authors develop a simple one-dimensional stochastic model of the interaction between spatially coherent atmospheric forcing patterns and an advective ocean. The model may be considered a generalization of the zero-dimensional stochastic climate model proposed by Hasselmann. The model equations are simple enough that they can be solved analytically, allowing one to fully explore the parameter space. The authors find that the solutions fall into two regimes: (i) a *slow–shallow* regime where local damping effects dominate and (ii) a *fast–deep* regime where nonlocal advective effects dominate. An interesting feature of the fast–deep regime is that the ocean–atmosphere system shows preferred timescales, although there is no underlying oscillatory mechanism in the uncoupled ocean or in the uncoupled atmosphere. Furthermore, the existence of the preferred timescale in the ocean does not depend upon a strong atmospheric response to SST anomalies. The timescale is determined by the advective velocity scale associated with the upper ocean and the length scale associated with low-frequency atmospheric variability. For the extratropical North Atlantic basin, this timescale would be of the order of a decade, indicating that advective ocean–atmosphere interaction could play an important role in decadal climate variability. The solutions also highlight the differences between local thermodynamic feedbacks associated with changes in the air–sea temperature difference and nonlocal dynamic feedbacks associated with horizontal ocean advection.

1. Introduction

The climate system exhibits variability on many timescales. Two simple models of the spectrum of climatic variability that are often used are white noise and red noise. For example, atmospheric spectra are often modeled as being white noise for timescales longer than a month or so (after filtering out the seasonal cycle). Hasselmann (1976) used such a model to argue that an important feature of the climate system is the red noise oceanic response to white noise atmospheric forcing. Neither white- nor red-noise spectra have any preferred timescales. However, real climatic spectra do show preferred timescales (or spectral peaks). Some of these preferred timescales are associated with periodicities in the external forcing, for example, the diurnal and annual cycles. Some others may be traced back to an intrinsic timescale associated with a single component of the climate system, such as the atmosphere or the ocean, with feedbacks from other components playing only a secondary role. An example is the Madden–Julian oscillation in the tropical atmosphere. The remaining preferred timescales of the climate system must arise through interactions between two or more components of the climate system, as in for example, the El Niño–Southern Oscillation (ENSO) phenomenon. Such timescales are associated with ''coupled'' modes of climatic variability, whereas the preferred timescales of a single component subsystem may be said to arise from ''uncoupled'' modes.

In recent years, there has been increasing attention devoted to climatic variability on decadal to centennial timescales. Understanding the mechanisms behind this variability is crucial to explaining regional climate shifts and also for distinguishing between natural and anthropogenic climate change. An important question regard-

* The National Center for Atmospheric Research is sponsored by the National Science Foundation.

Corresponding author address: R. Saravanan, National Center for Atmospheric Research, P.O. Box 3000, Boulder, CO 80307.
E-mail: svn@ncar.ucar.edu

ing decadal variability is whether there are any preferred timescales. Some observational studies suggest that there are indeed such timescales (e.g., Deser and Blackmon 1993; Levitus et al. 1994). A recent study by Sutton and Allen (1997) suggests that there may be a decadal timescale associated with the propagation of SST anomalies along the Gulf Stream. However, observational datasets are often too short in duration to allow definitive conclusions to be drawn.

Meanwhile, a variety of mechanisms have been put forward for selecting preferred timescales of decadal variability. Latif and Barnett (1994) have proposed a coupled mechanism that depends upon a rather strong atmospheric response to sea surface temperature (SST) anomalies. Many of the other proposed mechanisms are not so strongly coupled in nature and typically depend upon the existence of one or more oscillatory ocean modes. In some cases, the oscillatory ocean mode is unstable, and expresses itself spontaneously even with steady surface forcing (Weaver et al. 1991; Weaver and Sarachik 1991; Winton and Sarachik 1993). In other cases, all the oscillatory modes are damped, and stochastic forcing at the surface is required to excite them (Mikolajewicz and Maier-Reimer 1990; Mysak et al. 1993; Griffies and Tziperman 1995; Capotondi and Holland 1997; Saravanan and McWilliams 1997). The coupled general circulation model (GCM) study of Delworth et al. (1993) suggests that on multidecadal timescales, irregular oscillations of the oceanic thermohaline circulation may force atmospheric variability. A common feature of these oscillatory modes, whether damped or not, is that they appear to involve basin-scale interactions. A prototypical example of such a mechanism is the thermohaline ''loop'' oscillator described by Welander (1985). It is also possible that preferred timescales may be generated by local mechanisms, that is, not involving basin-scale interactions. For example, integration of white-noise freshwater fluxes over a localized region could generate decadal timescale variability (Weisse et al. 1994).

A related issue regarding variability on decadal timescales is the role of coupled versus uncoupled modes. In the Tropics, coupled modes seem to play a dominant role, at least on interannual timescales, but the situation in the midlatitudes is less clear. Only part of the midlatitude atmospheric variability appears to be related to coupled variability in the Tropics. For example, Hoerling et al. (1995) compared observations and ensemble GCM integrations and estimated that a significant fraction of the interannual low-frequency variability in the midlatitudes is due to ''internal'' dynamics, that is, unrelated to tropical SST variability. There is no clear consensus on the role of coupled ocean–atmosphere modes in the midlatitudes. Early studies of local ocean–atmosphere interaction (on monthly timescales) by Davis (1976) and Frankignoul and Hasselmann (1977) suggested a red-noise type of correlation between atmospheric forcing and SST patterns, with the ocean responding passively to atmospheric forcing. A recent study by Battisti et al. (1995), who used a mixed-layer model of the North Atlantic to simulate SST variability on interannual timescales, also concluded that atmospheric forcing of the ocean played the dominant role. The analyses of North Atlantic interannual variability coupled GCMs by Delworth (1996) and Saravanan (1998) also reached a similar conclusion. The idealized coupled model study of Saravanan and McWilliams (1997) concluded that spatial correlations in the atmospheric forcing played an important role. GCM studies of atmospheric response to realistic values of midlatitude SST anomalies find that the response is often quite weak, and sometimes inconsistent (e.g., Lau and Nath 1994). This is in contrast to the arguments of Latif and Barnett (1994) for the existence of coupled modes of variability. Yet another viewpoint is taken by some ocean modeling studies (e.g., Weaver et al. 1991; Weaver and Sarachik 1991), which tend to highlight the possible role of oceans in interdecadal variability.

In this study, we introduce a simple analytical model of advective ocean–atmosphere interaction, in a linear stochastic framework, to address some of the issues raised above. More complex numerical mixed-layer representations of the ocean, incorporating both stochastic forcing and advection, have been used to fit statistical models to observed data. Lemke et al. (1980) have fitted a stochastic model incorporating horizontal transport to observed polar sea-ice variability. Frankignoul and Reynolds (1983) describe the use of a local stochastic model, including the effects of advection by the observed mean current, to predict the statistical characteristics of observed SST anomalies in the North Pacific on timescales of several months. They find that mean advection has only a small effect in general, although in regions of large currents, the advection effects were important at lower frequencies. Herterich and Hasselmann (1987) have fitted a more general nonlocal stochastic model, incorporating advection and diffusion, to observed SST anomalies over the same region. In a different context, Penland and Matrosova (1994) have applied stochastic inverse modeling techniques to ENSO. Our goal, in contrast, is to use a simple model to explore the parameter space of coupled ocean–atmosphere interaction in the spirit of Hasselmann (1976) and identify the various regimes of advective ocean–atmosphere interaction.

One of the important results of this study is that advective ocean–atmosphere interaction can serve as a mechanism for selecting preferred timescales of variability. The mechanism acts over the region of atmospheric flux exchange with the ocean, and it does not require the presence of oscillatory modes either in the atmosphere or in the ocean. Our study also highlights the differences between local and nonlocal oceanic feedback to atmospheric forcing and its dependence on the coupling parameters. Section 2 briefly discusses aspects of the atmospheric and oceanic general circulation that

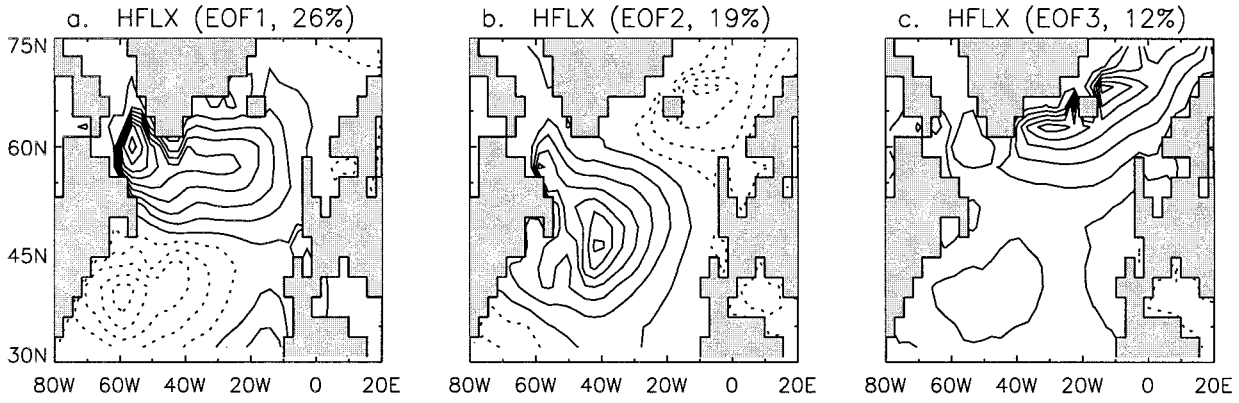

FIG. 1. The dominant EOFs of annually averaged surface heat flux into the North Atlantic computed from three 45-yr integrations of CCM3, forced by observed SST in the Tropics and climatological SST in the extratropics. The contour interval is 3 W m^{-2} (negative contours dashed). The fractional variance associated with each EOF is shown in the title.

motivate the one-dimensional model. Section 3 describes the model equations, properties of the white-noise forcing, and the analytical solution to the equations. The frequency spectrum of oceanic variability is discussed in section 4. The atmospheric variability spectrum and the role of oceanic feedback are analyzed in section 5, followed by concluding remarks in section 6.

2. Phenomenological motivation for the model

Consider midlatitude ocean–atmosphere interaction on decadal timescales. The associated spatial scales of interest are typically quite large, of the order of thousands of kilometers (Deser and Blackmon 1993; Kushnir 1994; Levitus et al. 1994). This is slightly smaller than gyre or basin scales in the ocean and somewhere in between planetary and synoptic scales in the atmosphere. Atmospheric variability on timescales of the order of a month or longer in the extratropics is characterized by the presence of a small number of large-scale ''standing wave'' modes with well-defined spatial structures, such as the well-known teleconnection patterns, the Pacific–North American (PNA) pattern and the North Atlantic Oscillation pattern (cf. Wallace and Gutzler 1981). In other words, low-frequency variability in the atmosphere is characterized by spatial coherence. In contrast, atmospheric variability on synoptic timescales (except for blocking events) tends to be spatially incoherent, as far as the slow-moving ocean is concerned; for example, there is no preferred spatial location for the ''highs'' and ''lows'' of an extratropical cyclone, such as there is for the PNA pattern. There are various theories that attempt to explain the origin of these patterns, based on barotropic energy dispersion, nearly stationary states of the atmosphere, instability of the climatological mean state, coherent feedback from the transient eddies, and so on (e.g., see Branstator 1992 and references therein).

The temporal evolution of these modes of low-frequency atmospheric variability is less well understood. Extended integrations of atmospheric models suggest these modes preserve their spatial structure over a broad band of frequencies (Nitsche and Wallace 1995). The variance spectrum of these modes appears to be essentially ''white'' for periods longer than one or two years (Feldstein and Robinson 1994; Nitsche and Wallace 1995; Saravanan and McWilliams 1995, 1997). In other words, uncoupled atmospheric variability on very long timescales is characterized by the lack of temporal coherence.

To illustrate the spatially coherent/temporally incoherent nature of intrinsic midlatitude atmospheric variability, we present some results from multidecadal integrations using a state-of-the-art atmospheric GCM. The model we use is the Community Climate Model, Version 3 (CCM3), developed at the National Center for Atmospheric Research (NCAR), which is described in Kiehl et al. (1996). We analyze three 45-yr integrations that were carried out using CCM3 at the standard T42 horizontal resolution, using observed SST values as the surface boundary condition in the tropical belt between 30°S and 30°N. The observed SST values used were derived from monthly mean values for the period January 1950–December 1994. Outside the tropical belt, the climatological annual cycle of SST was used as the surface boundary condition. (The observed and climatological SST values were blended over a 10°-wide transition region.) Therefore, all atmospheric variability in these integrations is either intrinsically generated or forced by tropical SST variability and is not related to any midlatitude SST variability.

The three 45-yr integrations of CCM3 were started from slightly different initial conditions, forming three independent realizations of the atmosphere. The annually averaged net surface heat flux into the North Atlantic region was computed for each of the 45 yr of the three integrations. Figure 1 shows the first three empirical orthogonal functions (EOFs) of the surface heat flux computed from the combined 135-yr dataset. The spatial structure of the EOFs as shown includes the variance information, so that the value at each grid point represents the typical root-mean-square (rms) heat flux deviation associated with the

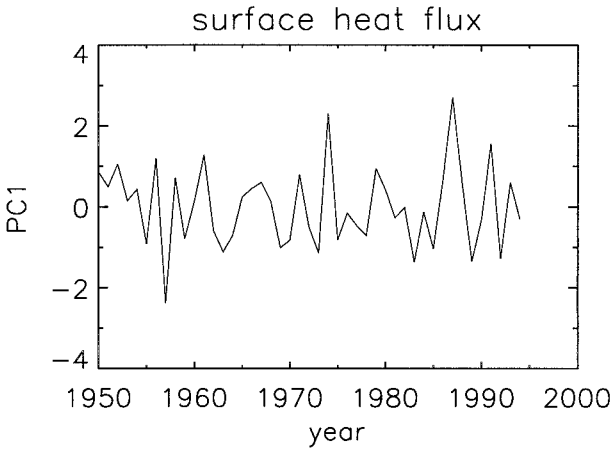

FIG. 2. The time series of the principal component associated with EOF1 of annually averaged surface heat flux shown in Fig. 1a. The time series has been normalized to have zero mean and unit variance.

EOF. These EOFs represent the intrinsic modes of extratropical surface forcing associated with the atmospheric variability, that is, in the absence of any oceanic feedbacks. Note that the three EOFs account for a significant fraction (57%) of the total variance and have fairly large-scale spatial structure, with maximum amplitudes biased toward the western part of the North Atlantic basin. Note also that the first two EOFs have dipolar structures, with the axis of the dipole oriented approximately parallel to the western boundary of the ocean basin. Similar north–south-oriented dipole patterns of heat flux variability have been noted in the hindcast study of North Atlantic SST variability by Battisti et al. (1995), in coupled GCM studies (Delworth 1996; Saravanan 1998), and also in the idealized coupled model study of Saravanan and McWilliams (1997). The time series of the principal component (or expansion coefficient) associated with EOF1 of surface heat flux is shown in Fig. 2 for one of the integrations. Although 45 yr of data are insufficient to definitively establish the spectral characteristics of the principal components, there is not much temporal coherence from year to year. (The other principal component time series show similar features.)

Next we consider the spatial structure of annually averaged SST variability in the North Atlantic region. We computed the EOFs of observed SST between the years 1903–94 using the GISST2 dataset (Rayner et al. 1995). The SST data were regridded on the CCM3 model grid, annually averaged, and the linear (least squares) trend was removed before the EOF computation. (There are trends in the dataset that may be attributable either to changes in the observing systems or to long-term climate change.) Figure 3 shows the first three EOFs of the annual mean SST. The EOFs show nearly basin-scale spatial structures, with the first having monopolar structure and the second and the third having dipolar structures. It is also interesting to note that these SST patterns are qualitatively similar to the spatial patterns seen in the surface heat flux EOFs (Fig. 1), although there are some phase differences in the spatial structures, and the patterns are ordered differently. The time series of the principal components associated with the EOFs of SST (not shown) exhibit interannual to interdecadal timescales. The spatial and temporal structure of observed interannual and longer timescale variability in the North Atlantic SST has been analyzed in detail in recent studies by Deser and Blackmon (1993), Kushnir (1994), and Battisti et al. (1995), who find similar patterns of variability. In particular, Deser and Blackmon (1993) suggest that there is a dipolar mode of SST variability associated with a timescale of about 10 yr. Several coupled modeling studies also find a dominant dipolar pattern of SST variability (Delworth 1996; Saravanan and McWilliams 1997; Saravanan 1998).

Stochastic models of SST variability (e.g., Hasselmann 1976; Frankignoul and Hasselmann 1977) have tended to emphasize the interaction between the atmosphere and the oceanic mixed layer on timescales of several months. Although such models may be appropriate for studying seasonal to interannual variability, oceanic variability on decadal and longer timescales is likely to involve parts of the ocean that lie below the mixed layer. For example,

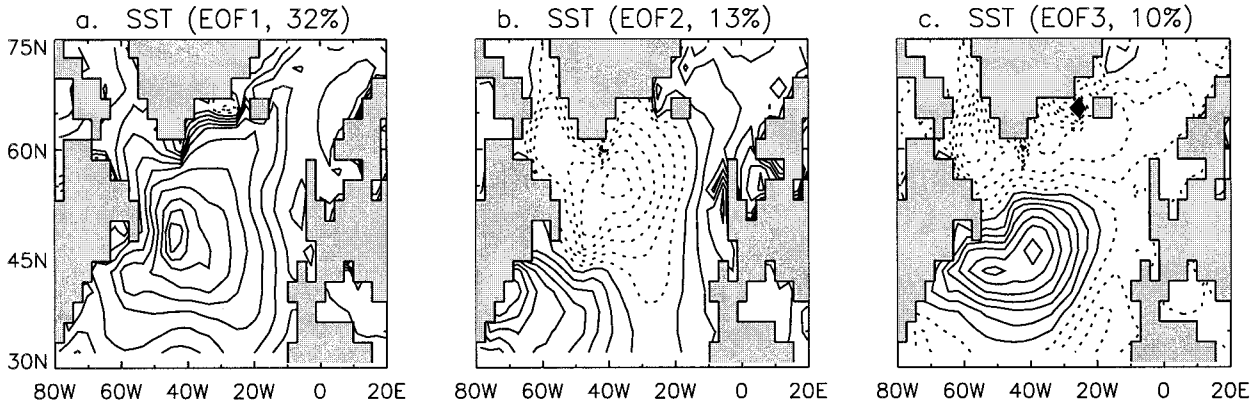

FIG. 3. The dominant EOFs of annually averaged SST in the North Atlantic computed from 92 yr (1902–94) of reconstructed observations from the GISST2 dataset. The contour interval is 0.05 K, and the fractional variance associated with each EOF is shown in the title.

Deser et al. (1996) find that the interdecadal variability signal in the central North Pacific originates at the surface and descends into the main thermocline to a depth of about 400 m. The advective role of the time–mean flow within the thermocline seems to be important in determining the evolution of the temperature anomalies. Levitus et al. (1994) found evidence for decadal patterns of variability at a depth of 120 m in the North Atlantic. Saravanan and McWilliams (1997) also found that the signal of interdecadal temperature variability in an idealized coupled model extended several hundred meters below the ocean surface. Stochastic models of interdecadal variability will have to take this relatively deep vertical structure and the role of time–mean advection into account.

To estimate the magnitude of the depth-averaged advective flow in the North Atlantic ocean, we turn to ocean GCMs, because it is difficult to find observational datasets of current measurements at various depths with enough spatial and temporal coverage to compute basin-wide climatologies. We analyzed the annual mean North Atlantic circulation in two different GCMs: (i) a ''coarse'' resolution (3° latitude–longitude grid) NCAR ocean model whose circulation is documented by Large et al. (1997), and (ii) a ''fine'' resolution (⅓°) model developed under the Community Modeling Effort (CME), whose circulation is documented in Bryan et al. (1995). Since the western boundary of the North Atlantic basin does not lie exactly along the north–south direction, we decomposed the horizontal velocity u into components (u^*, v^*), where u^* denotes the alongshore velocity (approximately parallel to the western boundary of the ocean basin) and v^* denotes the cross-shore velocity, that is, in the perpendicular direction. One may think of u^* as roughly corresponding to the velocity along the path of the Gulf Stream. Figure 4 shows u^*, vertically averaged over the top 500 m, for the annual mean circulation in the NCAR ocean model. (The great circle that defines the direction of u^* is also shown in the figure.) The values of u^* range from several centimeters per second near the Florida coast to a few centimeters per second after the boundary current separates.

Motivated by the spatial structure of the observed SST anomalies on interdecadal timescales (Fig. 3), we averaged u^* over a box encompassing the broad maxima shown in Fig. 4 and obtained a mean value of 2 cm s^{-1}. The length of the box (along the great circle) is 5000 km, giving a timescale of about 8 yr to transit along the length of the box. This advective timescale is at least an order of magnitude larger than what one would estimate from, say, the surface velocities associated with the narrow Gulf Stream jet. Sutton and Allen (1997), in their observational study of the propagation of SST anomalies along the path of the Gulf Stream, find a similar decadal advective timescale. We also estimated u^* using data from the fine-resolution CME model of the North Atlantic. Although the circulation in that model (not shown) has finer-scale features, the mean value of u^* over the aforementioned rectangular region is again about 2 cm s^{-1}.

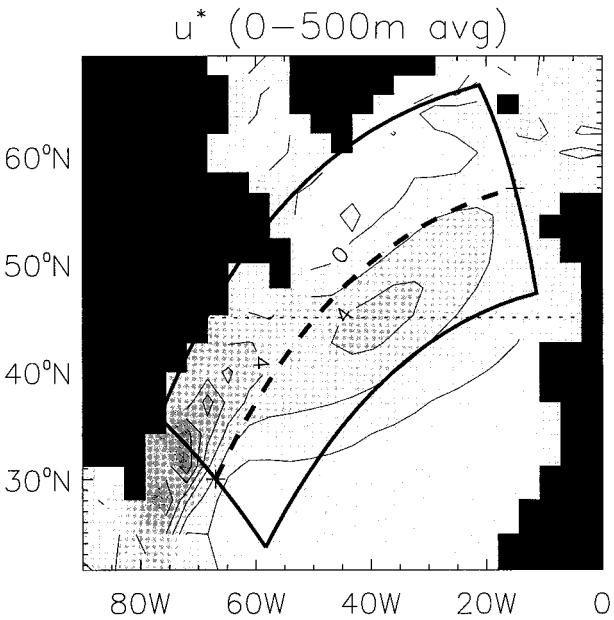

FIG. 4. Component of horizontal velocity (u^*) parallel to the great circle (dashed line) lying approximately along the western boundary of the basin (positive north-eastward), vertically averaged from the surface to 500-m depth. Computed from the annual mean circulation of the 3° × 3° NCAR Ocean Model. Average value of u^* in the ''box'' bounded by thick solid lines ≈2 cm s^{-1} (2 cm s^{-1} contours, with darker shading denoting more positive values).

3. Model formulation and solution

a. Model equations

We now construct a model of ocean–atmosphere interaction that explores the consequences of some of the important features of midlatitude climate variability on decadal timescales as noted above: the spatial coherence and temporal incoherence of atmospheric variability, the dipolar meridional structures in the surface heat fluxes, the relatively deep vertical structure of oceanic temperature anomalies, and the advective role of the ocean circulation.

Our model can be considered as being a heuristic representation of a basin-wide meridional dipole atmospheric pattern, such as the North Atlantic oscillation, interacting with the zonally averaged overturning circulation in the ocean (Fig. 5). Note that the thick line denoting the ocean circulation in Fig. 5 is not drawn as a closed loop, because we choose to restrict our attention to scenarios where the oceanic temperature anomalies are significantly attenuated over the time it takes for a complete circuit of the meridional overturning cell. For example, in three-dimensional circulations, surface water masses may be mixed or convected below the surface somewhere along the gyre and the effective circuit may be much longer than what the two-dimensional gyre streamlines would suggest. Furthermore, the overturning timescales associated with thermohaline circulations could be quite long, on the order of centuries. This motivates us to use inflow boundary conditions for the

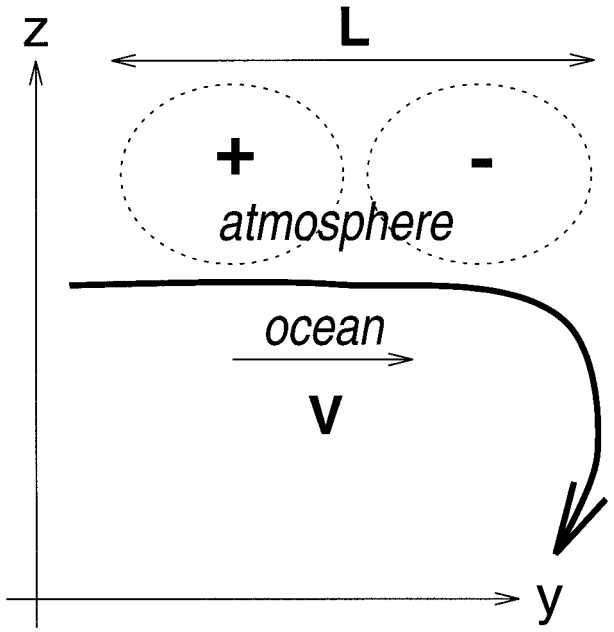

FIG. 5. Schematic of interaction between an atmospheric standing wave dipole pattern (dashed line) and an advective ocean circulation (thick solid line) in the zonally averaged vertical plane.

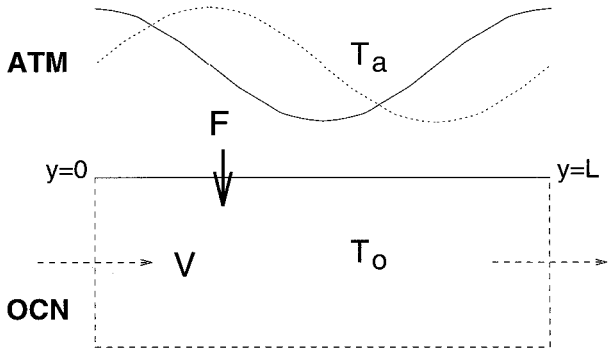

FIG. 6. Schematic of the ocean–atmosphere model. The solid and dotted curves denote the dominant modes of atmospheric variability. The shaded region represents the ocean, with the solid arrow denoting the surface heat flux and the dashed arrow denoting advection.

ocean model, so that unperturbed waters flow, into the localized region containing the atmospheric pattern, interact with it, and then flow out. In scenarios where there is memory associated with the gyre or overturning circulation, a reentrant boundary condition, incorporating delays and attenuation, would be more appropriate.

We consider a one-dimensional ''slab'' atmosphere along the meridional (y) direction, extending from $y = 0$ to L (Fig. 6). We take the atmosphere to be characterized by a single variable, its temperature T_a. One may think of it as representing the zonally and vertically averaged midlatitude atmosphere over an ocean basin, such as the region of the atmosphere over the extratropical North Atlantic basin (e.g., along the great circle shown in Fig. 4). Neglecting the zonal and vertical structure of atmospheric variability is a severe approximation and is made primarily for reasons of simplicity. The mean atmospheric flow in the midlatitudes is strongly zonal. According to the theory of quasi-stationary atmospheric waves (e.g., Held 1983; Frankignoul 1985), the relationship between SST anomalies and the associated atmospheric response is not necessarily local in the zonal direction. In fact, Frankignoul (1985) shows that the nonlocal nature of atmosphere–ocean interaction can sometimes give rise to eastward propagating SST anomalies, even in the absence of ocean advection. However, we have chosen to construct our one-dimensional model along the meridional direction, where the mean atmospheric flow is quite weak and the atmospheric response would tend to be more in phase with the SST anomaly.

Assume that the slab atmosphere exchanges heat with a one-dimensional slab ocean beneath it, having thickness H and temperature T_o. We prefer to use the term ''slab ocean,'' rather than call it a mixed layer, because we expect that on decadal timescales, layers of the real ocean beneath the mixed layer will also play a role in determining the variability (e.g., see Deser et al. 1996). Therefore, the slab ocean may be considered a vertically averaged representation of a portion of the upper ocean. An important process that we ignore is the role of vertical advection in the ocean. In particular, the slab ocean approximation would certainly break down in regions of deep convection. We assume further that the heat exchange between the atmosphere and the ocean is proportional to the local temperature difference between the two. This may not be too bad an approximation at large spatial scales in the atmosphere (see Frankignoul 1985). Note that this relationship does not necessarily imply that the maximum heating is in phase with the SST anomaly, because the atmospheric temperatures also need to be taken into account.

If we assume that the slab ocean is motionless, then there would be no nonlocal spatial interactions and we would essentially end up with a red-noise stochastic climate model of the kind described by Hasselmann (1976), with the spatial coherence of atmospheric variability simply being mirrored by the red-noise oceanic response. Horizontal advection in the ocean model permits nonlocal interactions and can lead to interesting deviations from a simple red-noise response. We consider the simplest form of oceanic advection—uniform advection in one dimension—and assume the slab ocean moves with a constant horizontal velocity, V. Henceforth, we shall use T_a, T_o to denote anomaly temperatures (i.e., deviations from a mean oceanic value), because advection of the mean ocean temperature by the mean circulation V does not affect the variability. At $y = 0$, we use the following inflow boundary condition for the ocean temperature anomaly T_o:

$$T_o(0, t) \equiv 0. \tag{1}$$

Following the approach taken by Hasselmann (1976), we may write the stochastic equations for the atmo-

spheric temperature anomaly $T_a(y, t)$ and the oceanic temperature anomaly $T_o(y, t)$ as follows:

$$\partial_t T_a = -\alpha T_a - \frac{F}{C_a} + \varepsilon_a(y, t), \tag{2}$$

$$\partial_t T_o = -V\partial_y T_o + \frac{F}{C_o} + \varepsilon_o(y, t), \tag{3}$$

and

$$F = \kappa(T_a - T_o), \tag{4}$$

where t denotes time, F is the heat flux into the ocean, and κ is an exchange coefficient relating the heat flux to the local air–sea temperature difference; C_a is the heat capacity of the atmosphere; $C_o = \rho_w C_w H$ is the heat capacity of the slab ocean, with ρ_w and C_w denoting the density and specific heat of water; α is an intrinsic damping coefficient for the atmosphere representing all dissipative processes except heat exchange with the ocean, which is represented by F; and ε_a and ε_o denote stochastic forcing of the atmosphere and the ocean, respectively. A similar one-dimensional set of equations, with the addition of a diffusive term but without the stochastic or advective terms, has been used by Marotzke and Pierce (1997) to model the interaction between a diffusive atmosphere and a slab ocean.

In addition to the intrinsic atmospheric damping coefficient α, it is convenient to define the auxiliary damping coefficients

$$\mu \equiv \frac{\kappa}{C_a} \quad \text{and} \quad \lambda \equiv \frac{\kappa}{C_o}, \tag{5}$$

where μ represents the damping of atmospheric temperature anomalies by heat exchange with the ocean and λ represents the damping of oceanic temperature anomalies by heat exchange with the atmosphere. This allows us to rewrite (2)–(4) as

$$(\partial_t + \alpha + \mu)T_a = \mu T_o + \varepsilon_a \quad \text{and} \tag{6}$$

$$(\partial_t + \lambda + V\partial_y)T_o = \lambda T_a + \varepsilon_o. \tag{7}$$

Although we shall be dealing with the nondimensional solutions to (6)–(7) and exploring regions of parameter space, it is useful to identify reference values for the model parameters so as to orient ourselves in parameter space. Estimates of the exchange coefficient κ are quite uncertain and scale dependent. We choose a value of 40 W m^{-2} K^{-1}, based on linearizations of bulk formulas for air–sea flux exchange (e.g., Haney 1971; Frankignoul 1985). This implies that $\mu^{-1} \approx 3$ days. The value of λ depends crucially on the choice of slab ocean thickness H. For typical mixed-layer thickness of about 50 m, we have $\lambda^{-1} \approx 2$ months. This would be appropriate for studying atmosphere–ocean interaction on seasonal to interannual timescales. On decadal timescales, the thermal variability in the ocean tends to have deeper vertical structure (e.g., Deser et al. 1996), and a larger value for the slab ocean depth would be more appropriate. For example, if $H = 500$ m (say), then $\lambda^{-1} \approx 20$ months. The advection velocity V would be a vertically averaged representation of oceanic flow over the thickness of the slab. For example, if we assume zonally averaged meridional transport of 20 Sverdrups (Sv) above 500 m depth in a basin that is 5000 km wide, then the associated zonal mean meridional velocity would be about 1 cm s^{-1}, which we choose to be a reference value for V. This may be appropriate for zonally averaged thermohaline flows but may be an underestimate when the wind-driven flow is also included (e.g., Fig. 4 suggests a somewhat higher value). For the domain length scale, we choose $L = 5000$ km, as suggested by the great circle path shown in Fig. 4.

We choose $C_a = 10^7$ J m^{-2} K^{-1}, which is the mass of the atmosphere times its specific heat per unit area. The intrinsic atmospheric damping timescale α represents a variety of dissipative processes such as horizontal eddy and mean flow heat transport and radiative heat loss to space. Estimates of its value range from a few days to several tens of days and are also scale dependent. Models of quasi-stationary waves in the atmosphere typically use damping timescales of 5–10 days to mimic the diffusive effects of transient eddies (Held 1983; Borges and Sardeshmukh 1995). For example, Lorenz (1973) estimates a decorrelation timescale of about 12 days for atmospheric states, and Branstator et al. (1993) estimate a timescale of about 6 days. This timescale differs considerably from those that are derived from eddy diffusion coefficients used in atmospheric energy balance models coupled to ocean models (Rahmstorf and Willebrand 1995; Marotzke and Pierce 1997). For spatial scales of O(5000 km) that we are interested in, arguments based on eddy diffusion coefficients for zonally averaged meridional heat fluxes would suggest a timescale of O(100 days) (e.g., Marotzke and Pierce 1997). One plausible explanation for this discrepancy is that it arises because the meridional eddy heat transport arguments ignore the predominantly zonal advective atmospheric heat transport—especially near the western boundaries of ocean basins—and may thus be underestimating the atmospheric dissipation. Zonally averaged fluctuations in the atmosphere tend to persist considerably longer than zonally asymmetric fluctuations. Therefore, the energy balance models may not be appropriate for modeling zonally asymmetric basin-scale ocean–atmosphere interaction on decadal timescales, such as in the vicinity of the North Atlantic basin, although they could be quite useful on longer timescales, such as the paleoclimatic timescales. Since we are primarily interested in modeling the very low-frequency atmospheric fluctuations associated with the quasi-stationary waves, we shall use the reference value $\alpha^{-1} = 9$ days, with the caveat that it is a rather uncertain value.

We will be interested in timescales of the order of years or longer. Since the atmospheric damping time-

scales are much shorter than that, we choose to use the following approximation to (6), for timescales $\gg \max(\alpha^{-1}, \mu^{-1})$:

$$(\alpha + \mu)T_a = \mu T_o + \varepsilon_a, \tag{8}$$

where the atmosphere is assumed to be in instantaneous equilibrium with the ocean temperature and the stochastic forcing. We then combine (7) and (8) to obtain a single governing equation for the ocean temperature:

$$(\partial_t + \lambda_{\text{eff}} + V\partial_y)T_o = \frac{\lambda_{\text{eff}}}{\alpha}\varepsilon_a + \varepsilon_o \quad \text{and}$$

$$\lambda_{\text{eff}} \equiv \frac{\lambda}{1 + (\mu/\alpha)}, \tag{9}$$

where λ_{eff} is the effective damping coefficient for the ocean when coupled to an interactive atmosphere. For the reference parameter values discussed above, we have $\mu/\alpha \approx 2$, giving $\lambda_{\text{eff}}^{-1} \approx 3\lambda^{-1}$. This means that coupling to an interactive atmosphere significantly reduces the SST anomaly damping timescale (as compared to an atmosphere with fixed properties). A somewhat similar effect was noted by Marotzke and Pierce (1997) in a coupled linear diffusive model. In their case, coupling the atmosphere to the ocean reduced the effective horizontal diffusivity by a factor, C_a/C_o, as compared to the horizontal diffusivity of the uncoupled atmosphere. This feedback is also seen in atmospheric GCM experiments with fixed anomalies, where the flux exchange coefficient κ may be effectively reduced from 40 W m^{-2} K^{-1} to about 20 W m^{-2} K^{-1} (e.g., Frankignoul 1985). For a shallow slab with $H = 50$ m, we have $\lambda_{\text{eff}}^{-1} \approx 6$ months, and for a deep slab with $H = 500$ m, we have $\lambda_{\text{eff}}^{-1} \approx 5$ yr.

Although stochastic forcing associated with mesoscale ocean eddies is likely to be important for mesoscale ocean variability (e.g., Voorhis et al. 1976), it is not clear whether it can play an important role on the basin scales that are of interest to us. Furthermore, the spatial and temporal characteristics of very low frequency variability in the ocean are less well known than of the atmosphere. In this study, for the sake of simplicity, we choose to set

$$\varepsilon_o(y, t) \equiv 0. \tag{10}$$

Since ε_a and ε_o appear additively on the rhs of (9), we should be able to easily generalize the results obtained using stochastic atmospheric forcing to the case with stochastic oceanic forcing as well.

For timescales $\ll \lambda_{\text{eff}}^{-1}$, it is instructive to consider the behavior of (9) in the limit of very small and very large values of V. Since we expect the atmospheric forcing to be spatially coherent and temporally incoherent, we take $\varepsilon_a(y, t) = W(t)f(y)$. In the slow advection limit ($V \to 0$), we may approximate (9) as

$$\partial_t T_o \approx \frac{\lambda_{\text{eff}}}{\alpha} W(t) f(y) \Rightarrow T_o \approx \frac{\lambda_{\text{eff}}}{\alpha} f(y) \int dt\, W(t). \tag{11}$$

The oceanic response is the time integral of the atmospheric forcing; for example, white-noise forcing would give a red-noise response (Hasselmann 1976). The spatial structure of the response is the same as that of the forcing. In the fast advection limit ($V \to \infty$), we may approximate (9) as

$$V\partial_y T_o \approx \frac{\lambda_{\text{eff}}}{\alpha} W(t) f(y) \Rightarrow T_o \approx \frac{\lambda_{\text{eff}}}{V\alpha} W(t) \int dt\, f(y). \tag{12}$$

The oceanic response is weak ($\propto V^{-1}$) and is the spatial integral of the atmospheric forcing. The temporal structure of the response is the same as that of the forcing. Note that there is a certain symmetry between the slow and fast advection limits, if we interchange the space and time coordinates.

b. White-noise forcing

The choice of the white-noise forcing term $\varepsilon_a(y, t)$ in (2) is motivated by the lack of temporal coherence seen in uncoupled atmospheric variability on very long timescales (e.g., Feldstein and Robinson 1994; Nitsche and Wallace 1995; Saravanan and McWilliams 1997). As for the spatial structure of ε_a, we consider atmospheric forcing with spatial structure $f(y)$ localized in the meridional domain $y = [0, L]$. We can expand $f(y)$ using a Fourier series as follows:

$$f(y) = a_o + \sum_{n=1}^{\infty} \{a_n \cos 2n\pi y + b_n \sin 2n\pi y\}. \tag{13}$$

We note that atmospheric variability tends to be dominated by a small number of spatial patterns, as discussed earlier (e.g., see Fig. 1). Therefore, we choose to consider two prototypical spatial structures for the forcing, $\cos(2\pi y/L)$ and $\sin(2\pi y/L)$ (Fig. 6). These would correspond to the first two terms with nontrivial spatial structure in the Fourier series expansion (13). Note that we can do this without loss of generality, because we are dealing with a linear system of equations. The atmospheric stochastic forcing is then expressed as

$$\varepsilon_a(y, t) = A_f(t) \cos\left(2\pi\frac{y}{L}\right) + B_f(t) \sin\left(2\pi\frac{y}{L}\right), \tag{14}$$

where A_f and B_f are independent Gaussian white-noise random variables, with zero mean, that represent the temporally incoherent nature of atmospheric forcing.

Note that because boundary condition (1) is not reentrant, there is no preferred timescale (or length scale) in the ocean model by itself, although there is a preferred velocity scale. Thus, mechanisms such as the loop oscillator described by Welander (1985) do not operate in this model. The atmospheric model too has no preferred timescale, although there is a preferred spatial scale of forcing. To anticipate one of the main conclusions of this study, we note that the oceanic velocity scale com-

bined with the atmospheric spatial scale can potentially give rise to a preferred timescale in the coupled system.

To describe the spectral properties of the white-noise forcing, we define the Fourier transform $\hat{f}(\nu)$ of a function $f(t)$ as follows:

$$\hat{f}(\nu) = \int_{-\infty}^{\infty} dt\, e^{-i2\pi\nu t} f(t) \quad \text{and}$$

$$f(t) = \int_{-\infty}^{\infty} d\nu\, e^{i2\pi\nu t} \hat{f}(\nu), \tag{15}$$

with ν denoting the frequency.

For any two stationary real time series $f(t)$ and $g(t)$, we may define the ensemble-average covariance cov(f, g; τ), with g lagging f by time τ, as follows:

$$\text{cov}(f, g; \tau) \equiv \langle f(t) g(t + \tau) \rangle, \tag{16}$$

where $\langle\rangle$ denotes ensemble averaging over different realizations of the random variables. Using the Fourier transform, (16) may be expressed as

$$\text{cov}(f, g; \tau) = \int_{-\infty}^{\infty} d\nu\, e^{i2\pi\tau\nu} \int_{-\infty}^{\infty} d\nu'\, e^{i2\pi t(\nu - \nu')} \langle \hat{f}^*(\nu') \hat{g}(\nu) \rangle, \tag{17}$$

with (*) denoting complex conjugation. We assume that the white-noise random variables A_f and B_f satisfy the following:

$$\langle \hat{A}_f^*(\nu') \hat{A}_f(\nu) \rangle = \hat{a}^2 \delta(\nu' - \nu),$$

$$\langle \hat{B}_f^*(\nu') \hat{B}_f(\nu) \rangle = \hat{b}^2 \delta(\nu' - \nu), \tag{18}$$

where $\hat{a}$ and $\hat{b}$ are constants representing the strengths of the cosine/sine components of white-noise forcing and δ denotes the Dirac delta function.

In principle, one could use (17) and (18) to compute covariances analytically, usually through contour integration in the complex plane. In practice, however, (17) turns out to be too cumbersome to use in all but the simplest of covariance computations, because the expressions for the resulting analytical contour integrals are rather complicated. We find it much easier to evaluate covariances using a discretized Fourier transform version of (17). The integrand $\langle \hat{f}^*(\nu') \hat{g}(\nu) \rangle$ typically falls off quite rapidly as $|\nu| \to \infty$, so that the discretized version of (17) converges fairly quickly. Details of this discretization are given in appendix A.

c. Scaling and solution

The simplicity of the coupled model described above allows analytical solution of the governing equations. To find the general solution to (9), it is convenient to apply the Fourier transform, which gives the following equation for $\hat{T}_o(y, \nu)$:

$$\left[1 + 2\pi \frac{V}{L\lambda_{\text{eff}}} \left(i\frac{\nu L}{V} + \frac{L}{2\pi} \partial_y \right) \right] \hat{T}_o = \frac{\hat{\varepsilon}_a}{\alpha}. \tag{19}$$

The form of (19) motivates us to nondimensionalize all lengths by L, and all timescales by the advective timescale $\mathcal{T}_{\text{adv}} \equiv L/V$. Temperature is assumed to be scaled by a temperature scale $\mathcal{T}_{\text{scale}}$, which does not need to be explicitly specified because our equations are linear in T. The surface heat flux F will be scaled by κT_{scale}. It is convenient to scale the stochastic forcing ε_a by αT_{scale}, although this means that the nondimensionalized stochastic forcing amplitude cannot be considered to be constant if α is allowed to vary. *Hereafter, all variables may be assumed to be nondimensional, unless otherwise stated.*

After substituting the Fourier transform of (14) in (19) and nondimensionalizing, we obtain

$$\left[1 + \Gamma \left(i\nu + \frac{1}{2\pi} \partial_y \right) \right] \hat{T}_o = \hat{A}_f(\nu) \cos(2\pi y) + \hat{B}_f(\nu) \sin(2\pi y). \tag{20}$$

The nature of the solutions to (20) is essentially controlled by a single nondimensional parameter Γ, defined by

$$\Gamma \equiv \frac{\omega_{\text{adv}}}{\lambda_{\text{eff}}}, \qquad \omega_{\text{adv}} \equiv \frac{2\pi}{\mathcal{T}_{\text{adv}}}. \tag{21}$$

For the choice of parameter values $L = 5000$ km, $V = 1$ cm s^{-1}, the characteristic advective timescale $\mathcal{T}_{\text{adv}} \approx 16$ yr. For the North Atlantic, the relevant horizontal velocity scale may be at least twice as large (Fig. 4), implying a timescale of about 8 yr. This suggests that advection will play an important role primarily on decadal or longer timescales. If we take the atmospheric properties to be fixed, Γ can be thought of as representing the ratio of the strength of horizontal advection to the thermal inertia of the ocean (i.e., the slab thickness). Therefore, we may refer to Γ as the ''advection–damping ratio.'' We anticipate the following two regimes of behavior for the solutions to (20): (i) A *slow–shallow* regime corresponding to $\Gamma \ll 1$, where the depth of penetration of thermal anomalies is small and thermal damping effects dominate over advection; and (ii) a *fast–deep* regime corresponding to $\Gamma \gg 1$, where thermal anomalies penetrate quite deeply and the thermal damping effects are weaker than advection. For $\lambda_{\text{eff}} = 2$ yr and $V = 1$ cm s^{-1}, the values of Γ can range from 0.25 to 2.5 for values of H ranging from 100 m to 1000 m, thus straddling both regimes. We note from (9) that λ_{eff} is quite sensitive to the choice of the atmospheric damping timescale α^{-1}; hence the range of interest for Γ is even larger. Since we have chosen a fairly short timescale for our reference value of α^{-1}, a longer timescale would imply a larger value of Γ.

The form of the boundary condition (1) motivates the

use of the Laplace transform in the y direction, defined by

$$\tilde{f}(y) \equiv \int_0^\infty dy\, e^{-sy} \hat{f}(y). \tag{22}$$

Transforming (20), we obtain an equation for $\tilde{T}_o(s, \nu)$:

$$\left[1 + \Gamma\left(i\nu + \frac{s}{2\pi}\right)\right]\tilde{T}_o = \frac{\hat{A}_f s + \hat{B}_f 2\pi}{s^2 + 4\pi^2}. \tag{23}$$

Here we have extended the model domain to $0 \le y < \infty$ to simplify the computations. Since there is no upstream influence in this model, this does not make any difference to the solution in the domain $0 \le y \le 1$. The inverse Laplace transform of (23) can be computed quite easily by contour integration in the complex s plane (Dennery and Krzywicki 1967) around the poles $s = i2\pi, -i2\pi, -2\pi\xi$, where

$$\xi \equiv \frac{1}{\Gamma} + i\nu. \tag{24}$$

The solution is given by

$$\hat{T}_o(y, \nu) = \frac{1}{\Gamma(1 + \xi^2)} \times \{\hat{A}_f[\xi \cos 2\pi y + \sin 2\pi y - \xi e^{-\xi 2\pi y}] + \hat{B}_f[\xi \sin 2\pi y - \cos 2\pi y + e^{-\xi 2\pi y}]\}. \tag{25}$$

The first two terms in the square brackets of (25) do not decay in the y direction and represent the local response to the forcing. The third term in the square brackets, which is proportional to $\exp(-2\pi y/\Gamma)$, may be thought of as being the ''spatial transient response'' to a forcing turned on at $y = 0$.

We note that there is a certain degree of symmetry between the response to cosine forcing ($\hat{A}_f$) and the response to sine forcing ($\hat{B}_f$) in (25). For simplicity we shall henceforth restrict ourselves to the case with zero cosine forcing. Furthermore, since we are dealing with a linear system, we may choose the sine forcing to have unit amplitude, that is, we choose the following parameters for the nondimensional version of (18):

$$\hat{a}^2 = 0, \qquad \hat{b}^2 = 1. \tag{26}$$

In other words, we shall restrict our attention to the oceanic response to a ''dipole'' atmospheric forcing of the form $\sin(2\pi y)$ from now on. Appendix B discusses sensitivity of the oceanic variability to this choice by considering monopole and tripole structures for the forcing as well.

4. Oceanic variability

a. Nodes and antinodes

First we consider the solution to (25)–(26) for $\nu = 0$, that is, the response to stationary (time invariant) atmospheric forcing. As we see in Fig. 7, the ensemble-average zero-frequency oceanic response, $\langle|\hat{T}_o(y, 0)|^2\rangle$, is characterized by nodes and antinodes, that is, locations with zero variance and locations with a local maximum in the variance, respectively. For $\Gamma \ll 1$, when advective effects are not important, the nodes of the oceanic response essentially coincide with the nodes of the $\sin(2\pi y)$ atmospheric forcing function. However, for $\Gamma \ge O(1)$, the nodes of the oceanic response are shifted downstream with respect to the forcing. For example, for $\Gamma = 1/16$ and $1/4$, the interior node is located at $y \approx 0.5$, whereas it is located at $y = 0.76$ for $\Gamma = 4$, about a quarter ''wavelength'' downstream of the node in the forcing function.

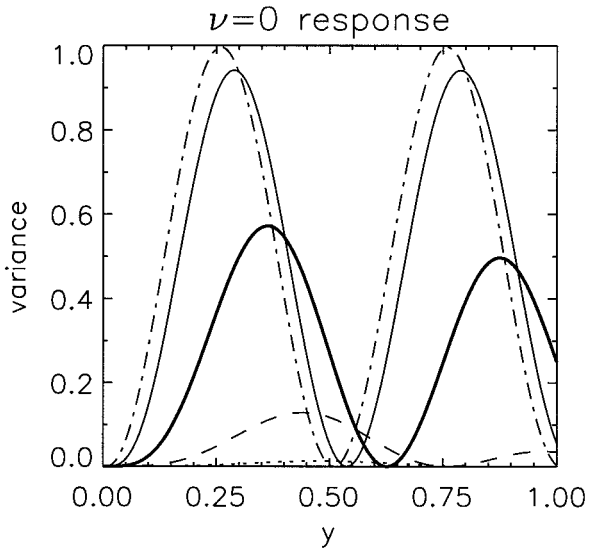

FIG. 7. Ensemble-averaged zero frequency variance of oceanic temperature ($\langle|\hat{T}_o(y, 0)|^2\rangle$) for dipole atmospheric forcing, as a function of y for different values of Γ. [Dot–dash, thin solid, thick solid, dashed, dotted lines denote $\Gamma = 1/16$, $1/4$, 1, 4, 16 cases, respectively. That is, dot-dash and thin solid lines correspond to the slow–shallow regime; dashed and dotted lines correspond to the fast–deep regime; thick solid line corresponds to the intermediate value $\Gamma = 1$].

The existence of nodes of the zero-frequency response has implications for the frequency spectrum of the oceanic response. In the nodal regions, the response cannot simply be described as being either red noise or white noise, since both types of spectra have nonzero variance as $\nu \to 0$. Figure 8a shows the frequency spectrum $\langle|\hat{T}_o(y_0, \nu)|^2\rangle$ at the interior node at $y_0 = 0.76$ for $\Gamma = 4$. Note that the nodal spectrum is nonmonotonic and shows maximum variance at $\nu \approx 1$, although the atmospheric forcing has a white-noise spectrum. That is, there is a preferred timescale associated with the oceanic response at the nodal region. In contrast, the frequency spectrum at the nearby antinode ($y_0 = 0.44$) shows a more typical red-noise structure with no preferred timescales, as would be expected from the arguments of Hasselmann (1976). Thus we see that when advective effects are important and the atmospheric

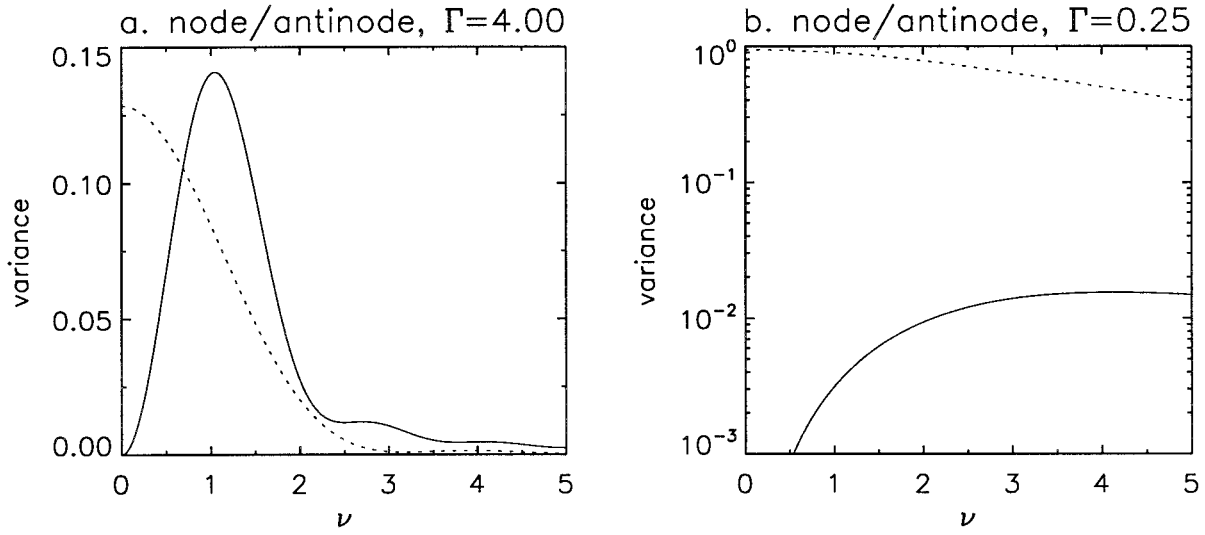

FIG. 8. Ensemble-averaged frequency spectrum of oceanic temperature variance ($\langle|\hat{T}_o(y_0, \nu)|^2\rangle$) at a node (solid) and the neighboring antinode (dotted): (a) $\Gamma = 4$ (node at $y_0 = 0.76$; antinode at $y_0 = 0.44$); (b) $\Gamma = 1/4$ (node at $y_0 = 0.54$; antinode at $y_0 = 0.29$).

variability is spatially coherent, the spectral characteristics of the oceanic variability can be spatially inhomogeneous, differing significantly from red noise in certain regions. This inhomogeneity is most apparent for $\Gamma \gtrsim 1$. For smaller values of Γ, the nodal response is much weaker than the antinodal response and is therefore not very significant (Fig. 8b).

b. Frequency spectrum

Consider the oceanic response over all frequencies. We define σ_o^2, the total variance of T_o integrated over all frequencies, as follows:

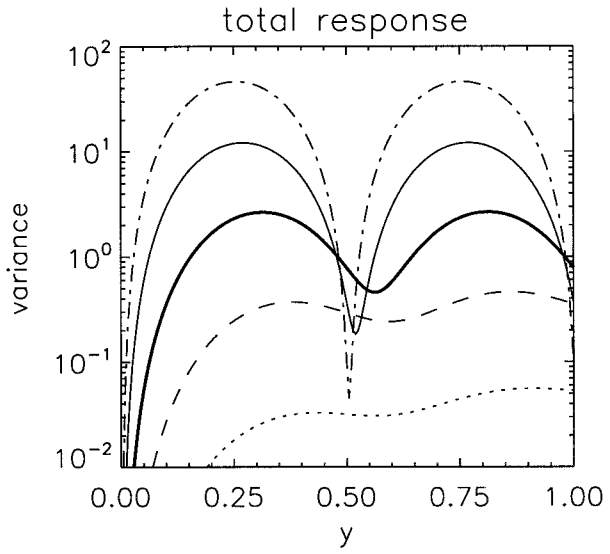

FIG. 9. Spatial structure of oceanic temperature variance integrated over all frequencies, $\sigma_o^2(y)$, for $\Gamma = 1/16$, $1/4$, 1, 4, 16. (Lines as in Fig. 7.)

$$\sigma_o^2(y) = \int_{-\infty}^{\infty} d\nu \langle|\hat{T}_o(y, \nu)|^2\rangle. \tag{27}$$

The spatial structure of σ_o^2 and its Γ dependence are shown in Fig. 9. Note that the amplitude of the oceanic variance decreases very rapidly with increasing Γ. For $\Gamma \ll 1$, the structure of σ_o^2 essentially reflects dipolar atmospheric forcing, with a minimum in variance at $y \approx 0.5$. For $\Gamma \gg 1$, σ_o^2 has an almost monotonic spatial structure, with a narrow region of rapid initial increase in variance downstream of $y = 0$, followed by a rather slow increase farther downstream.

The spatial structure of σ_o^2 for $\Gamma \geq O(1)$ as seen in Fig. 9 does not suggest any natural way to decompose the oceanic response into different modes. Unlike the $\sin(2\pi y)$ atmospheric forcing function, the oceanic response does not satisfy any simple boundary condition at $y = 1$. However, we recall that our choice of the atmospheric forcing function was motivated by a Fourier series expansion in the interval $y = [0, 1]$ (13). This motivates us to try and decompose the frequency-dependent oceanic response $\hat{T}_o(y)$ using a Fourier series expansion in the interval $y = [0, 1]$. Such an expansion should allow us to study how the oceanic feedback affects the atmospheric variability, because we will be using the same basis functions for both the atmospheric and the oceanic variables. Note that since the oceanic response is not periodic, the Fourier expansion will have to deal with a jump discontinuity at $y = 0$. We shall evaluate a posteriori the convergence properties of such an expansion, as measured by whether a small number of modes capture a large fraction of the variance.

The Fourier expansion of $\hat{T}_o(y, \nu)$, as given by (25)–(26) may be written as

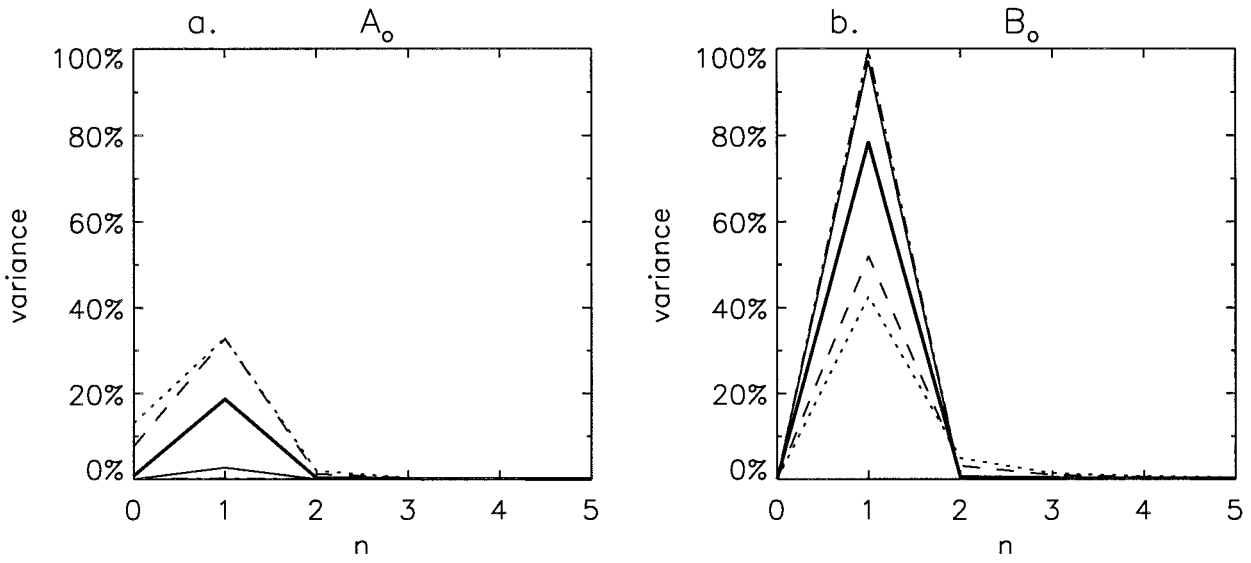

FIG. 10. Fractional oceanic temperature variance associated with different meridional wavenumbers n in the interval $0 < y < 1$, integrated over all frequencies, for $\Gamma = 1/16, 1/4, 1, 4, 16$: (a) even (cosine) components; (b) odd (sine) components. (Lines as in Fig. 7.)

$$\hat{T}_o(y, \nu) = \hat{A}_o^{(0)}(\nu) + \sum_{n=1}^{\infty} \{\hat{A}_o^{(n)}(\nu) \cos 2n\pi y + \hat{B}_o^{(n)}(\nu) \sin 2n\pi y\}, \qquad (28)$$

where n denotes the "meridional wavenumber." The Fourier components $\hat{A}_o^{(n)}$ and $\hat{B}_o^{(n)}$ may be computed from (25) as

$$\hat{A}_o^{(n)}(\nu) = \frac{-\hat{B}_f}{\Gamma(1 + \xi^2)} \frac{1}{(1 + \delta_{n,0})} \left\{ \delta_{n,1} - \xi \frac{1 - e^{-2\pi\xi}}{\pi(n^2 + \xi^2)} \right\}$$

and

$$\hat{B}_o^{(n)}(\nu) = \frac{\hat{B}_f}{\Gamma(1 + \xi^2)} \left\{ \xi \delta_{n,1} + n \frac{1 - e^{-2\pi\xi}}{\pi(n^2 + \xi^2)} \right\}, \qquad (29)$$

where $\delta_{nn'}$ denotes the Kronecker delta function.

Recall that the atmospheric white-noise forcing (14) is confined to meridional wavenumber $n = 1$. However, the oceanic response can be spread over a range of meridional wavenumbers, because advection can create spatial structures that differ from the $\sin(2\pi y)$ forcing structure. Figure 10 shows the variance associated with the different Fourier components $\hat{A}_o^{(n)}$ and $\hat{B}_o^{(n)}$, integrated over all frequencies ν using (17) and expressed as a fraction of the total $\hat{T}_o$ variance, $\int dy\ \sigma_o^2(y)$. We see that in the slow–shallow regime, almost all the variance is concentrated in $\hat{B}_o^{(1)}$, that is, the response has the same structure as the forcing. In the fast–deep regime, the fractional variance associated with $\hat{B}_o^{(1)}$ diminishes to about 40% or less, and the fractional variance associated with $\hat{A}_o^{(1)}$ increases significantly, appearing to saturate around 30%. There is also some "leakage" of variance into the higher meridional wavenumbers, but it is quite small for $\Gamma \leq 16$. Nevertheless, $\hat{A}_o^{(1)}$ and $\hat{B}_o^{(1)}$ together capture a large fraction of the total variance of $\hat{T}_o$, for a range of Γ values. Therefore, we focus on the two dominant modes of oceanic response to atmospheric forcing: the *direct* mode of response $\hat{B}_o^{(1)}$ and the spatially *orthogonal* mode of response $\hat{A}_o^{(1)}$. Hereafter, we shall denote them simply as $\hat{B}_o$ and $\hat{A}_o$, respectively. That is,

$$\hat{A}_o(\nu) \equiv \hat{A}_o^{(1)}(\nu); \qquad \hat{B}_o(\nu) \equiv \hat{B}_o^{(1)}(\nu). \qquad (30)$$

There are two ways to explain the presence of an orthogonal mode of response. One being that in the limit of very fast advection, as discussed in section 3a, the oceanic response is the spatial integral of the atmospheric forcing, $B_f \sin 2\pi y$. Another interpretation is that the oceanic response is a propagating mode, which would project onto two spatially orthogonal standing wave modes. The presence of orthogonal modes of oceanic response raises some interesting possibilities, because these oceanic modes can, in turn, excite orthogonal atmospheric modes. This means that oceanic advection can mediate interactions between spatially orthogonal atmospheric modes. It also means that the coupled ocean–atmosphere system is likely to include modes of the uncoupled atmosphere *plus* the corresponding orthogonal modes. Of course, the strength of the orthogonal atmospheric response will depend on the strength of the ocean–atmosphere coupling.

We now consider the frequency-variance spectrum $\langle|\hat{B}_o(\nu)|^2\rangle$ and $\langle|\hat{A}_o(\nu)|^2\rangle$ of the direct and orthogonal modes of response. In the slow–shallow regime, the direct mode shows a red-noise type of spectrum that flattens out as $\nu \to 0$ (Fig. 11a). The overall variance of the direct mode decreases monotonically with increasing Γ. In the fast–deep regime, the overall direct response is weaker by an order of magnitude or more, but there is a broad peak in the vicinity of $\nu = 1$. In

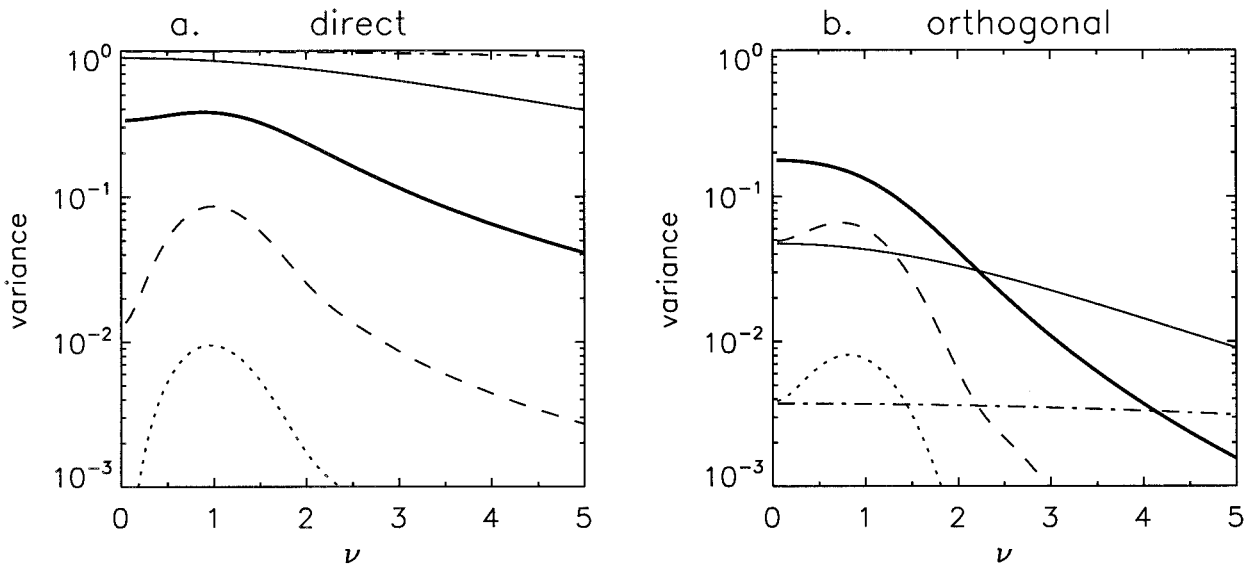

FIG. 11. Frequency spectrum of oceanic temperature variance associated with the direct and orthogonal modes of response, for $\Gamma = 1/16, 1/4, 1, 4, 16$: (a) $\langle|\hat{B}_o(\nu)|^2\rangle$ (b) $\langle|\hat{A}_o(\nu)|^2\rangle$. (Lines as in Fig. 7.)

other words, the fast–deep regime shows a preferred frequency corresponding to the timescale L/V. One may think of this preferred frequency as arising from a kind of ''advective resonance,'' because if one were to apply periodic boundary conditions at $y = 0, 1$, one would get truly resonant behavior for $\nu = 1$. The orthogonal mode (Fig. 11b) shows a similar tendency for frequency selection in the fast–deep regime, but the spectral peak near $\nu = 1$ is less pronounced. Interestingly, the maximum orthogonal response occurs not for $\Gamma \to 0$ or for $\Gamma \to \infty$, but for $\Gamma = 1$, that is, the orthogonal mode seems to be most efficiently excited for $\Gamma = O(1)$. The phase relationship between the atmospheric forcing and the direct/orthogonal modes of oceanic response is discussed in appendix C.

One often tends to associate spectral peaks in the variance of a dynamical system with the existence of oscillatory normal modes. We have shown above that stochastically forced advective ocean–atmosphere interaction can result in spectral peaks in the oceanic variance, even when there are no identifiable oscillatory normal modes of the uncoupled or coupled systems. However, the spectral peak is discernible only for sufficiently large value of the advection–damping ratio, that is, $\Gamma \gtrsim 1$. Depending upon the actual advection/damping ratio in different regions of the ocean, this frequency selection mechanism may or may not turn out to be important. As suggested by Fig. 4, the advective timescale for the North Atlantic upper ocean is of the order of a decade. By the arguments of section 3a, Γ is likely to be of O(1) or even larger. This means that the frequency selection mechanism discussed above could play a role in decadal variability in the North Atlantic.

5. Atmospheric variability

a. Frequency spectrum

We now focus on how the feedback associated with the oceanic response affects the atmospheric variability itself. Using the nondimensional Fourier-transformed versions of (4) and (8), scaled as described in section 3c, we may write the total atmospheric response $\hat{T}_a(y, \nu)$ and the surface flux $\hat{F}(y, \nu)$ as

$$\hat{T}_a = \frac{\hat{\varepsilon}_a + (\mu/\alpha)\hat{T}_o}{1 + (\mu/\alpha)} \quad \text{and} \tag{31}$$

$$\hat{F} = \frac{\hat{\varepsilon}_a - \hat{T}_o}{1 + (\mu/\alpha)}. \tag{32}$$

(Recall that the scaling for the stochastic forcing includes the factor α.) The first numerator term in the rhs of (31) represents the direct atmospheric response to white-noise forcing in the absence of the ocean, whereas the second numerator term and the denominator are due to feedback from the ocean. Since $\hat{T}_o$ and $\hat{\varepsilon}_a$ are correlated, as discussed in the previous section, the two terms can ''interfere'' constructively or destructively with each other, depending upon their relative complex phase. The relative contribution of the oceanic feedback to overall atmospheric variability is controlled by the ratio μ/α, which we may refer to as a ''coupling parameter.'' It is the ratio of the intrinsic atmospheric damping timescale to the timescale for heat exchange with the ocean. The case $\mu/\alpha \ll 1$ would correspond to weak coupling, and the case $\mu/\alpha \gg 1$ to strong coupling between the atmosphere and the ocean. (Recall that our choice of reference values for μ and α, as discussed in section 3a, imply a reference value of $\mu/\alpha \approx 3$.)

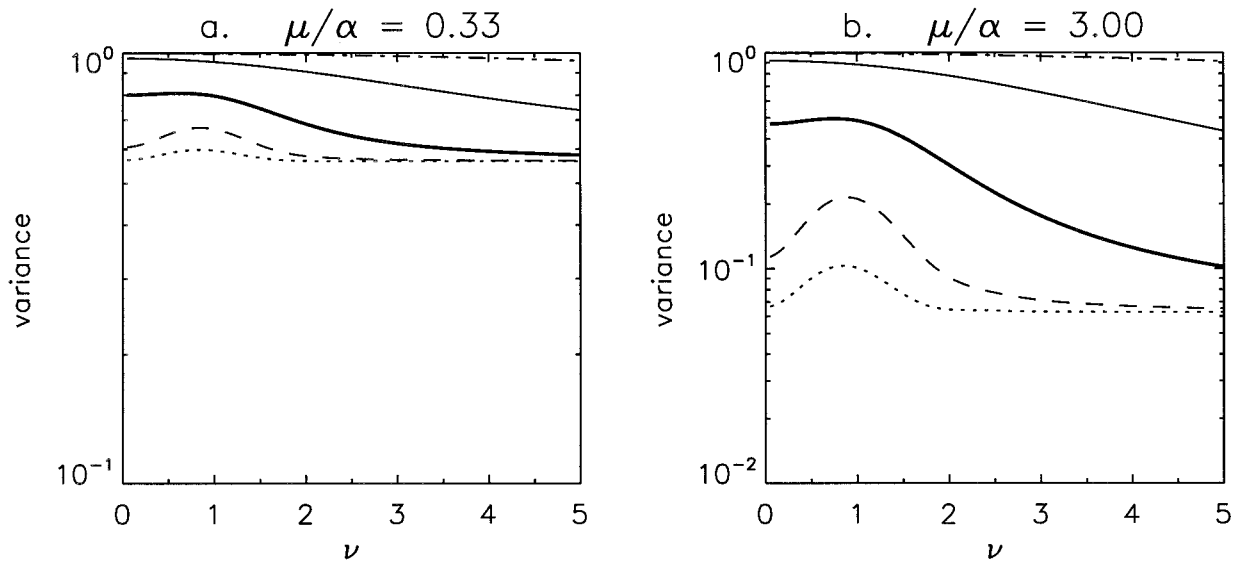

FIG. 12. Frequency spectrum of atmospheric temperature variance associated with the direct mode, $\langle|\hat{B}_a(\nu)|^2\rangle$, for $\Gamma = 1/16, 1/4, 1, 4, 16$: (a) $\mu/\alpha = 1/3$, (b) $\mu/\alpha = 3$. (Lines as in Fig. 7.)

We may decompose $\hat{T}_a(y, \nu)$ using a Fourier series expansion in the interval $0 < y < 1$, as in (28), to obtain the contributions from different meridional wavenumbers n, $\hat{A}_a^{(n)}(\nu)$ and $\hat{B}_a^{(n)}(\nu)$. Restricting ourselves to the dipole-forcing case $\hat{a}^2 = 0$, $\hat{b}^2 = 1$, as in the previous section, we shall once again make the identification $\hat{B}_a(\nu) \equiv \hat{B}_a^{(1)}(\nu)$, which would correspond to the direct mode of atmospheric variability, with $\sin(2\pi y)$ structure, and $\hat{A}_a(\nu) \equiv \hat{A}_a^{(1)}(\nu)$, corresponding to the orthogonal mode of atmospheric variability, with $\cos(2\pi y)$ structure. Using (31) and the linearity of the Fourier series expansions, $\hat{B}_a$, $\hat{A}_a$ may be expressed as

$$\hat{B}_a = \frac{\hat{B}_f + (\mu/\alpha)\hat{B}_o}{1 + (\mu/\alpha)} \quad \text{and} \tag{33}$$

$$\hat{A}_a = \frac{(\mu/\alpha)\hat{A}_o}{1 + (\mu/\alpha)}, \tag{34}$$

where we have assumed for the sake of simplicity that $\hat{A}_f \equiv 0$, that is, there is no atmospheric forcing with $\cos(2\pi y)$ structure. (If such forcing did exist, and were coherent with $\hat{B}_f$, it could lead to more complex interactions than are considered here.) From (34) we see that the orthogonal mode of atmospheric variability is simply a scaled version of the orthogonal mode of oceanic response shown in Fig. 11b. The direct mode of atmospheric variability is more interesting, because it interacts with the oceanic direct mode.

Since the direct mode of oceanic response shows a preferred frequency in the fast–deep regime, we may ask whether this is reflected in the atmospheric variability. Figure 12 shows the frequency spectrum of the direct mode of atmospheric response, $\langle|\hat{B}_a(\nu)|^2\rangle$ for $\mu/\alpha = 1/3$, 3. In the slow–shallow regime, we see weak monotonic decay in power with increasing ν, indicating red-noise type of behavior. In the fast–deep regime, there is a significant peak near $\nu = 1$ and white-noise structure for $\nu \to \infty$. The amplitude of the peak decreases with increasing Γ, with the peak being most prominent for $\Gamma = O(1)$. The value of μ/α does not seem to affect the qualitative structure of the spectra in the slow–shallow regime. However, in the fast–deep regime, the overall variance level decreases with increasing μ/α, and the spectral peak becomes more prominent. One may think of the frequency spectrum for the fast–deep regime as consisting of a white-noise direct atmospheric response to stochastic atmospheric forcing, with a peak arising from the oceanic feedback superimposed on it. The strength of the oceanic feedback, like the oceanic variability, decreases with increasing Γ. However, its relative strength, compared to the direct atmospheric response to stochastic forcing, increases with increasing μ/α.

Next we consider the direct mode of the surface heat flux $\hat{B}_F$, which may be computed using (32) and Fourier decomposition as

$$\hat{B}_F = \frac{\hat{B}_f - \hat{B}_o}{1 + (\mu/\alpha)}. \tag{35}$$

Figure 13 shows the frequency spectrum of $\hat{B}_F$ for $\mu/\alpha = 3$. It is interesting to note that, in a sense, the $\hat{B}_F$ spectrum is the ''mirror image'' of the corresponding $\hat{B}_a$ spectrum (Fig. 12b), with elevated levels of atmospheric temperature variability corresponding to decreased surface flux amplitudes and vice versa. In particular, the $\hat{B}_F$ spectrum is rather like ''blue noise'' for $\Gamma \gg 1$ (the slow–shallow regime). This simply reflects the fact that the air–sea temperature gradient $(T_a - T_o)$ approaches zero for timescales longer than the damping timescale $(\lambda_{\text{eff}}^{-1})$ associated with the slab ocean. Of course, the deep ocean has much longer timescales as-

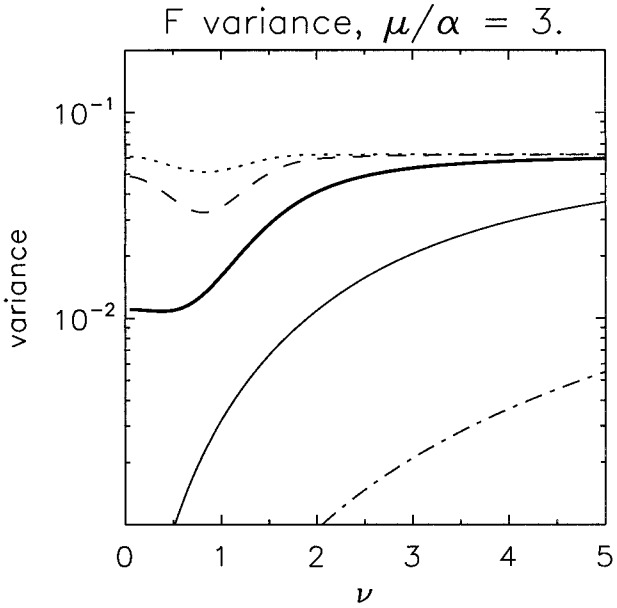

FIG. 13. Frequency spectrum of surface heat flux variance, $\langle|\hat{B}_F(\nu)|^2\rangle$, associated with the direct mode of oceanic response for $\mu/\alpha = 3$ and $\Gamma = 1/16$, $1/4$, 1, 4, 16. (Lines as in Fig. 7.)

sociated with it, which may mask the blue-noise spectrum associated with the slab ocean response. For $\Gamma \gg 1$, the $\hat{B}_F$ spectrum is more like white noise, but with a trough at $\nu \approx 1$, corresponding to the peak in $\hat{B}_a$ spectrum. This should not be too surprising since a decrease in the surface heat flux would imply decreased thermal damping of atmospheric temperature anomalies, allowing them to be more persistent.

To summarize, the frequency selection mechanism that characterizes the oceanic response in the fast–deep regime expresses itself in the atmospheric variability, through oceanic feedback associated with the surface fluxes. However, the spectral peak near $\nu = 1$ tends to be less prominent in the atmospheric frequency spectrum, because it is superimposed upon a strong white-noise background. This means that it will be more difficult to detect a statistically significant spectral peak in the atmospheric variables than in the oceanic variables.

b. Types of oceanic feedback

There are two different types of oceanic feedback that can affect the atmospheric variability in our simplified model of ocean–atmosphere interaction.

1) LOCAL FEEDBACK

This is a thermodynamic feedback that would occur even in the absence of ocean advection. If there is a positive atmospheric temperature anomaly over a region of uniform SST, the associated air–sea temperature difference would result in positive heat flux into the ocean and lead to the formation of a positive SST anomaly. This would result in a decreased air–sea temperature difference, and hence decreased surface heat fluxes, and increased persistence of the atmospheric temperature anomaly. This feedback can explain features such as the increase in overall atmospheric temperature variance associated with decreased surface heat flux amplitudes (Figs. 12b, 13). A recent study by Barsugli and Battisti (1998) presents a detailed discussion of this feedback. However, this local feedback cannot by itself explain the emergence of a spectral peak in the atmospheric variability for $\Gamma \gg 1$ (Fig. 12).

2) NONLOCAL FEEDBACK

This is a dynamic feedback where ocean advection plays an important role. The ''constructive interference'' between the spatial patterns of T_a and T_o that gives rise to the spectral peak in T_a variance (for the direct mode) is an example of such a feedback. The timescale at which this occurs is determined by the length scale associated with the atmospheric forcing and the velocity scale associated with the ocean advection. Another example of this type of feedback would be the atmospheric response to orthogonal modes of ocean variability, which would have a different spatial structure from the original atmospheric forcing.

The local feedback described above can easily be explored in the case with no advection ($V \equiv 0$). Since it is somewhat difficult to understand the parameter dependence of the overall variability amplitudes using the nondimensional equations, because parameters such as α appear in several places, *we temporarily revert to the dimensional form of the equations.* We consider two limits: (i) infinite heat capacity ocean ($C_o \to \infty$) and (ii) zero heat capacity ocean ($C_o \to 0$). Case (i) can be considered as representing an atmospheric model forced by prescribed SST at the surface, because the ocean acts like an infinite heat reservoir. Case (ii) can be considered as representing an atmospheric model coupled to a very shallow mixed layer. For case (i), we may approximate (8) as

$$T_a \approx \frac{\varepsilon_a}{\alpha + \mu},$$

because $T_o \to 0$ as $C_0 \to \infty$ for finite F. For case (ii), we may approximate (8) as

$$T_a \approx \frac{\varepsilon_a}{\alpha},$$

because $F \to 0$ as $C_o \to 0$. Thus, the atmospheric variability would be proportional to $(\alpha + \mu)^{-2}$ for an infinite heat capacity ocean and proportional to α^{-2} for a zero heat capacity ocean. In other words, one would expect an atmospheric model coupled to a mixed layer to show more variability (but weaker surface heat fluxes) than an atmospheric model forced by prescribed SST. Such an effect has been noted on decadal timescales in an idealized ocean–atmosphere model (Saravanan and

McWilliams 1997). Marotzke and Pierce (1997) have also highlighted the role of finite oceanic heat capacity in determining the damping timescales of thermal anomalies.

c. *Forcing the atmosphere with ''observed'' SST: AMIP-style integrations*

Consider now a conceptual experiment where we carry out a long integration with our coupled ocean–atmosphere model. We use the ''SST'' from such an integration as the lower boundary condition for a subsequent integration of a stand-alone atmospheric model, with different initial conditions. Integrations of this kind have been carried out by the Atmospheric Model Intercomparison Project (AMIP) using realistic atmospheric general circulation models and observed SST. Therefore, we shall refer to the stand-alone atmospheric integration described above as an AMIP-style integration. We then ask the following questions: (i) How well does the AMIP-style integration capture the amplitude of variability in the coupled integration? (ii) How well does the AMIP-style integration capture the correlations between the atmospheric flow and the SST?

In our simple atmospheric model, the total atmospheric response $\hat{T}_a(y, \nu)$ for the AMIP-style integration can be expressed quite simply by rewriting (31) as

$$(\hat{T}_a)_{\text{AMIP}} = \frac{\hat{\varepsilon}_a + (\mu/\alpha)(\hat{T}_o)_{\text{coupled}}}{1 + (\mu/\alpha)}, \tag{36}$$

where $(\hat{T}_o)_{\text{coupled}}$ represents the time series of SST from the coupled integration and is a surrogate for the observed SST used in an AMIP integration.

An important question is whether the statistical properties of $\hat{\varepsilon}_a$, the stochastic atmospheric forcing, depend significantly on the SST variability. Studies of the atmospheric response to prescribed midlatitude SST anomalies indicate that the response is rather weak (e.g., Lau and Nath 1994). There are also statistically significant relationships between midlatitude atmospheric variability and tropical SST anomalies; however, ensemble GCM integrations indicate that much of the interannual atmospheric variability in the midlatitudes may nevertheless be ''intrinsic,'' that is, independent of any SST variability (Hoerling et al. 1995). This suggests that to a first approximation, we may assume that the statistical properties of $\hat{\varepsilon}_a$ depend only on the climatology of SST, which is the same for both the coupled and AMIP-style integrations. In other words, we assume that $\hat{\varepsilon}_a$ is statistically independent of $(\hat{T}_o)_{\text{coupled}}$, that is, $\langle \hat{\varepsilon}_a^*(\nu')(\hat{T}_o(\nu))_{\text{coupled}} \rangle \equiv 0$, but otherwise has the same statistical properties as in the coupled integration.

As in the previous section, we restrict ourselves to the dipole-forcing case $\hat{a}^2 = 0$, $\hat{b}^2 = 1$. Using the analog of (33), we may write the frequency-variance spectrum of the direct mode of atmospheric response as

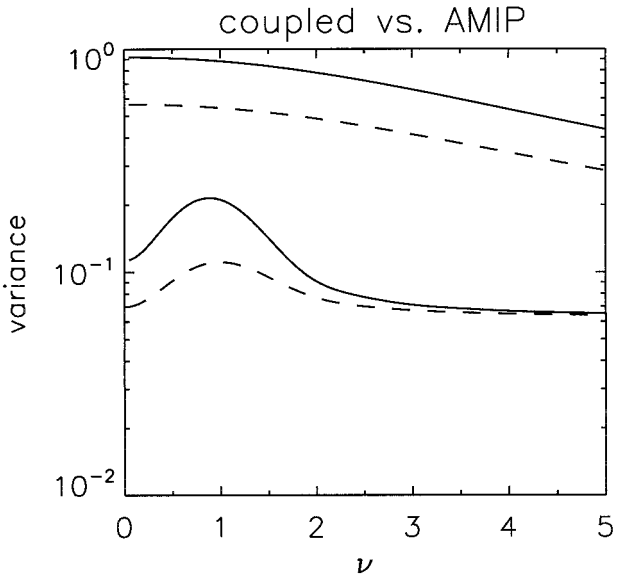

FIG. 14. Frequency spectrum of atmospheric temperature variance associated with the direct mode, $\langle|\hat{B}_a(\nu)|^2\rangle$, for coupled (solid) and AMIP-style (dashed) integrations, with $\Gamma = \frac{1}{4}$ (thick) and $\Gamma = 4$ (thin) ($\mu/\alpha = 3$ case).

$$\langle|\hat{B}_a(\nu)|^2\rangle_{\text{AMIP}} = \frac{1 + (\mu/\alpha)^2\langle|\hat{B}_o(\nu)|^2\rangle_{\text{coupled}}}{[1 + (\mu/\alpha)]^2}. \tag{37}$$

The first term in the numerator of the above expression represents the unit variance associated with the white-noise forcing and the second term represents the scaled variance associated with the SST from the coupled integration. The terms appear additively because the cross term involved in computing the modulus of the rhs of (36) vanishes due to the assumed statistical independence of $\hat{T}_o$ and $\hat{\varepsilon}_a$. In the limit $\mu/\alpha \to 0$, the intrinsic atmospheric variability dominates. In the limit $\mu/\alpha \to \infty$, atmospheric variability forced by the SST dominates. In both limits—trivially for the first limit, and by design for the second—the AMIP-style integration should provide a good estimate of the variability in the coupled integration. However, this may not necessarily be true for $\mu/\alpha = \text{O}(1)$. Figure 14 shows the frequency-variance spectrum of the direct mode of atmospheric response, for the coupled and AMIP-style integrations. For $\nu = \text{O}(1)$, we see that the AMIP-style integration underestimates the variability for $\Gamma = \frac{1}{4}$. For $\Gamma = 4$, the AMIP-style integration estimates the high-frequency ($\nu \gg 1$) variability fairly well but significantly attenuates the spectral peak near $\nu = 1$ seen in the coupled integration. For $\nu \to \infty$, the AMIP-style integration should provide a good estimate of the variability in the coupled integration, because the SST tends to be in quadrature with the atmospheric forcing (Fig. C1).

Consider a stochastically excited positive T_a anomaly in the coupled integration. Through surface flux exchange, this would tend to produce a positive T_o anomaly. In doing so, the air–sea temperature gradient ($T_a -$

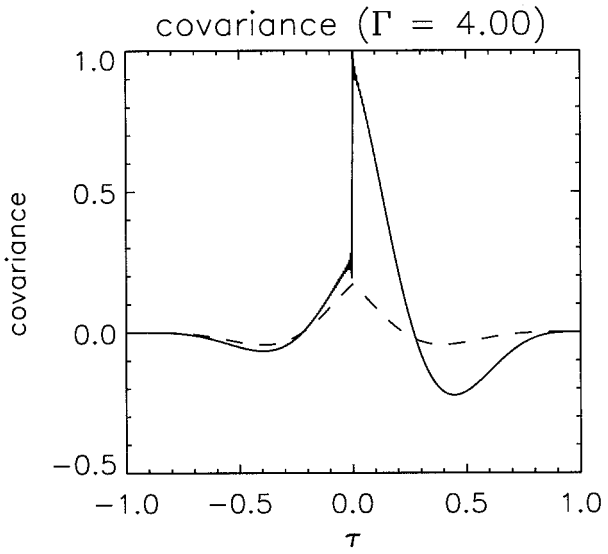

FIG. 15. Normalized covariance between the oceanic and atmospheric direct modes of variability, cov($\hat{B}_a$, $\hat{B}_o$; τ), for the direct mode in the coupled (solid) and AMIP-style (dashed) integrations, for Γ = 4 and μ/α = 3. (Both covariances have been normalized by the maximum absolute covariance in the coupled integration.)

T_o) and the associated surface heat flux would be reduced, thus allowing the T_a anomaly to persist longer. However, specifying the same T_o anomaly in the AMIP-style integration does not permit this interaction to occur, because the SST is not allowed to vary in response to the atmospheric forcing. This means that the statistics of atmospheric variability in the AMIP-style integration will not necessarily be identical to that of the coupled integration. This point is also made in the study by Barsugli and Battisti (1998).

The normalized covariance cov($\hat{B}_a$, $\hat{B}_o$; τ) between the atmospheric and oceanic direct modes is shown in Fig. 15 for the coupled and AMIP-style integrations. The maximum absolute value of the covariance in the coupled integration is used as the common normalization factor. For the AMIP-style integration, the covariance actually has the same structure as the autocovariance of the coupled SST variability, cov($\hat{B}_o$, $\hat{B}_o$; τ), because the SST is uncorrelated with the atmospheric white-noise forcing. For the coupled integration, the covariance is a weighted sum of cov($\hat{B}_f$, $\hat{B}_o$; τ) and cov($\hat{B}_o$, $\hat{B}_o$; τ). We see that the AMIP-style integration tends to underestimate the covariance at lag zero and almost misses out the negative minimum in the covariance near $\tau \approx 0.4$ seen in the coupled integration.

6. Summary and discussion

On interannual and longer timescales, intrinsic (i.e., uncoupled) extratropical atmospheric variability appears to be fairly well described by a white-noise frequency spectrum (Feldstein and Robinson 1994; Nitsche and Wallace 1995; Saravanan and McWilliams 1997). One may think of very low frequency atmospheric variability as random ''climate noise'' arising from high-frequency daily weather fluctuations. We can therefore approximate it as having stochastic time dependence, even though the equations of motion may themselves be deterministic. Although it may have no preferred timescales, very low frequency atmospheric variability is dominated by a small number of preferred spatial structures (cf. Wallace and Gutzler 1981). In this study, we have constructed a one-dimensional stochastic ocean–atmosphere model that explores the consequences of the aforementioned features of atmospheric variability. The model also incorporates the effect of horizontal advection by the time–mean ocean circulation, which could play a significant role in climate variability on decadal and longer timescales.

The simplicity of the one-dimensional model implies that some important atmospheric and oceanic processes are neglected. In particular, nonlocal atmospheric processes, such as zonal advection, are not explicitly considered. However, those nonlocal atmospheric processes that interact to produce the spatially coherent patterns of low-frequency variability are implicitly included through the stochastic forcing parameterization. This means that even fluctuations in the boundary layer heat and moisture transports that are ultimately responsible for the surface heat flux anomalies are implicitly included, to the extent that they are driven by the large-scale atmospheric low-frequency variability.

The equations governing the one-dimensional stochastic model are simple enough that they may be solved analytically using Laplace and Fourier transforms. It turns out that the nature of the analytical solutions is essentially controlled by a single nondimensional parameter, the advection–damping ratio Γ, which measures the strength of horizontal ocean advection in relation to the thermal damping effects. Depending upon the value of Γ, the solutions to the one-dimensional model fall into two regimes: (i) the *slow–shallow* regime ($\Gamma \ll 1$) where advection effects are weak and the oceanic variability can be described as being red-noise (Hasselmann 1976), and (ii) the *fast–deep* regime ($\Gamma \gg 1$), where horizontal advection dominates over thermal damping. We note that the thermal damping timescale of the ocean would increase with increasing depth, because of increased heat capacity. Therefore, shallow structures of temperature variability in the ocean would correspond to the first regime, and deeper structures would correspond to the second regime. Deser et al. (1996) suggest that oceanic temperature variability on decadal timescales could extend over several hundred meters of depth in the ocean, which would imply weaker thermal damping.

The qualititative difference in the time evolution of oceanic temperature anomalies for the two regimes is

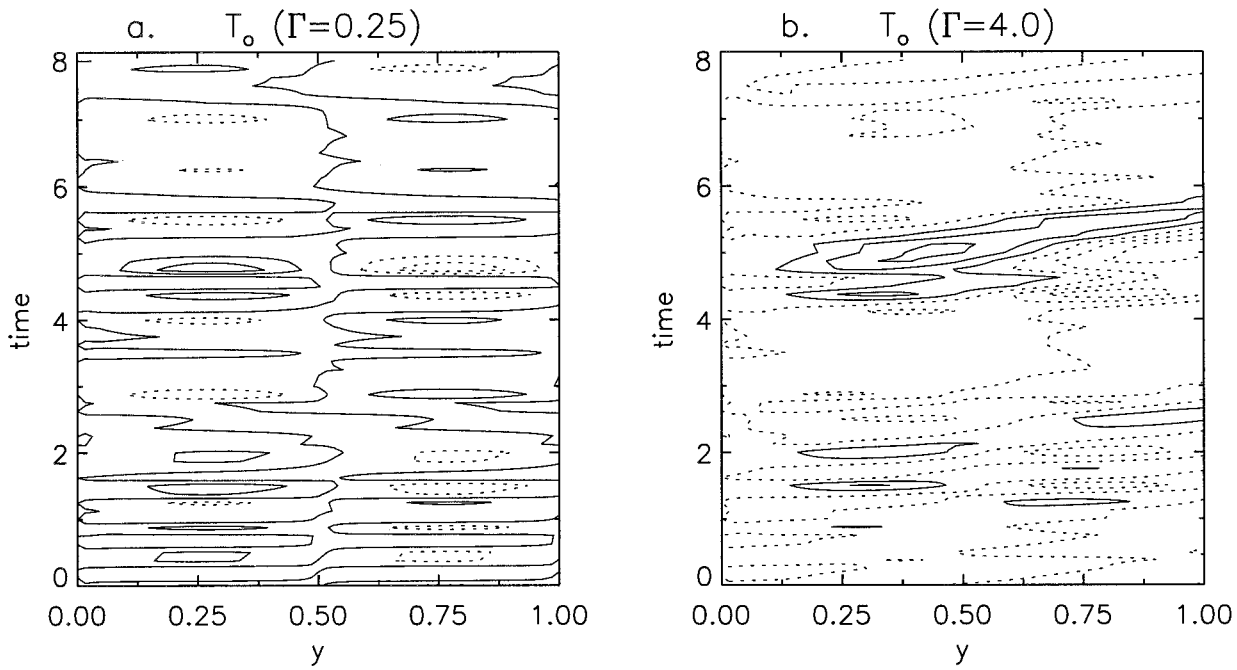

FIG. 16. Time evolution of nondimensional oceanic temperature (T_o) in a single realization of the stochastic model (computed numerically): (a) $\Gamma = \frac{1}{4}$ (slow–shallow regime), contour interval = 0.25; (b) $\Gamma = 4$ (fast–deep regime), contour interval = 0.04. {The abscissa corresponds to the nondimensional spatial coordinate [unit length = O(5000 km)], and the ordinate corresponds to the nondimensional time [unit time = O(10 yr)]. Dashed contours denote negative values.}

shown in Fig. 16, for two values of Γ. Here we have numerically solved the equations of the analytical model to produce a single realization of the stochastic time evolution of oceanic temperature for each value of Γ. (The analytical results represent the average over an ''infinite'' ensemble of such numerical solutions.) Note that for the slow–shallow regime (Fig. 16a), the spatial structure of oceanic temperature variability simply reflects the dipolar standing wave atmospheric forcing. In the fast–deep regime (Fig. 16b), one can clearly see advected features in the oceanic temperature variability, corresponding to a nondimensional timescale of O(1). However, given the stochastic nature of the system, there is no precise time period associated with the variability.

An interesting feature of the fast–deep regime is that the spectrum of oceanic variability can no longer be simply described as being red noise; there is actually a spectral peak in the variability corresponding to the advective timescale $\mathcal{T}_{adv} = L/V$, where V is the horizontal advective velocity scale in the ocean and L is a length scale associated with atmospheric variability. The spectral peak tends to be more prominent in the oceanic variability than in the atmospheric variability; the strong background white-noise variability makes it more difficult to detect the peak in the atmosphere. It is worth noting that in our simple model, neither the atmosphere nor the ocean, when uncoupled, supports oscillatory modes of variability. The preferred timescale of variability arises only when the atmosphere and the ocean are coupled.

A heuristic explanation of the rigorous analytical results for the origin of the preferred timescale is shown in Fig. 17. Consider a dipolar standing wave pattern of atmospheric variability with white-noise temporal structure. This may be viewed in spectral space as a random superposition of oscillations with all possible periods. Let us focus on the component with period L/V. At time $t = 0$, the atmospheric forc-

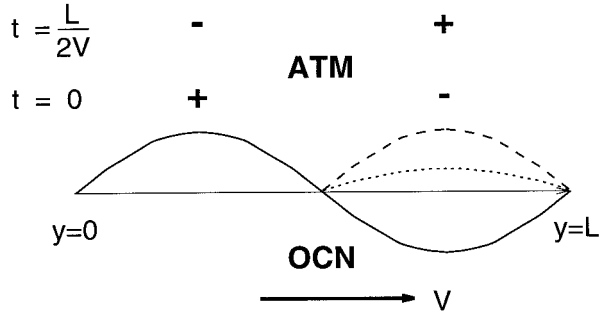

FIG. 17. Schematic illustration of the mechanism behind the preferred timescale L/V. Plus/minus signs denote the sign of the surface heat flux associated with atmospheric forcing at time $t = 0$ and a ''half-period'' later ($t = L/2V$). Solid sinusoidal curve shows the structure of the SST anomaly at $t = 0$. Dashed curve shows the SST anomaly at $t = L/2V$, for the fast–deep regime, with weak damping effects. Dotted curve shows the SST anomaly at $t = L/2V$, for the slow–shallow regime, with strong damping effects.

ing would excite an SST anomaly shown by the solid sinusoidal curve. At $t = L/2V$, in the fast–deep regime, the SST anomaly would be displaced by a distance $L/2$, as shown by the dashed curve. At the same time, the spectral component of atmospheric forcing with period L/V would also have changed sign, leading to positive reinforcement of the SST anomaly. Of course, white-noise atmospheric forcing would also contain spectral components at all other possible periods, but these would not interact coherently with the ocean. In the slow–shallow regime with strong damping effects, the SST anomaly would be significantly attenuated at $t = L/2V$, as shown by the dotted curve. Therefore, the positive reinforcement effect would be less important.

There are several different ways in which preferred timescales can arise in extratropical oceanic variability. As discussed in the introduction, it can occur through unstable modes of extratropical air–sea interaction, or through oscillatory modes of the oceanic circulation. We argue that advective ocean–atmosphere interaction can also serve as a mechanism for generating preferred timescales in the ocean. This mechanism, unlike many other mechanisms, does not rely upon having a strong atmospheric response to midlatitude SST anomalies. It is not based upon a closed atmosphere–ocean ''feedback loop,'' but simply on spatially coherent atmospheric forcing of an advective ocean. Of course, this mechanism generates preferred timescales only if the advection–damping ratio $\Gamma \gtrsim 1$. For example, in the idealized coupled model study of Saravanan and McWilliams (1997), the advective velocity scale is about 0.6 cm s^{-1} and the depth scale for the thermal anomalies is about 500 m, which implies that $\Gamma \approx 0.75$. This means that the effects of damping are marginally stronger than that of advection, and nonlocal oceanic feedback is likely to be somewhat weak, making it difficult to detect any preferred timescales associated with this feedback. However, for the upper oceanic circulation for the extratropical North Atlantic (say over the top 500 m), using an advective velocity scale of 2 cm s^{-1} (e.g., see Fig. 4), suggests that $\Gamma \gtrsim 2.5$, depending upon the intrinsic atmospheric damping scales. The associated advective timescale is of O(10 yr). This suggests that advective ocean–atmosphere interaction could potentially play an important role in decadal climate variability in the North Atlantic region. It is interesting to note that the time evolution of oceanic temperatures in the fast–deep regime of our stochastic model (Fig. 16b) bears a qualitative resemblance to the observed time evolution of SST anomalies along the path of the Gulf Stream, as described in the study by Sutton and Allan (1997). Perhaps this model could explain the advective propagation of SST anomalies and the preferred decadal timescales noted in their study.

The one-dimensional coupled model simulates not only the characteristics of the oceanic response to atmospheric forcing, but also the effects of the feedback from the ocean on atmospheric variability. The strength of this feedback is controlled by the coupling parameter μ/α, which is the ratio of the intrinsic atmospheric damping timescale α^{-1} to the timescale for heat exchange with the ocean μ^{-1}. There are two types of oceanic feedback that affect the atmospheric variability. *Local feedback*: when the ocean responds to atmospherically generated surface heat flux anomalies by forming SST anomalies, it results in reduced air–sea temperature gradients and decreased surface heat flux; this means that atmospheric thermal anomalies with the same structure as the SST anomalies tend to be more persistent. *Nonlocal feedback*: SST anomalies produced by atmospheric forcing can be horizontally advected by the oceanic flow and produce an atmospheric response elsewhere. The nature of this nonlocal feedback would depend upon the strength and spatial structure of the ocean circulation.

The strength of the local feedback described above would depend upon the effective heat capacity of the ocean. The larger the oceanic heat capacity, the smaller the SST response to surface heat fluxes and hence a weaker feedback. In the limit of infinite heat capacity, which corresponds to prescribed SSTs, the feedback would vanish. On timescales of the order of several months, the effective oceanic heat capacity can be taken to be the same as that of the mixed layer. However, on longer timescales, oceanic layers below the mixed layer and advective–diffusive processes that damp thermal anomalies would also play a role in determining the effective oceanic heat capacity.

The role of the effective oceanic heat capacity in determining the surface heat flux variability brings up some interesting issues with regard to the so-called AMIP type of integrations, where observed SSTs are used as the surface boundary condition for extended integrations of an atmospheric GCM. The hope is that using these ''perfect'' surface boundary conditions should enable the atmospheric model to faithfully simulate the variability of the coupled ocean–atmosphere system. However, the atmosphere is forced by surface fluxes of heat and moisture, and not directly by the SST. Specifying the SST is just a convenient way of getting these fluxes right. This is guaranteed to work when the evolution of SST is deterministic, as in the seasonal cycle, for example. However, part of the observed SST variability may itself be a response to nondeterministic (stochastic) atmospheric forcing. Specifying this response component of SST variability as the boundary condition for an atmospheric model integration will not reproduce the original atmospheric forcing conditions.

In our simple coupled model, we are able to carry out AMIP-type integrations analytically, by using the statistical distribution of SSTs derived from the analytical coupled integrations to force the uncoupled version of the

simple atmospheric model. The coupling parameter μ/α plays an important role in determining how well the AMIP-type integrations can capture the true coupled variability. In the limit $\mu/\alpha \to \infty$, the AMIP-type integrations do reproduce true coupled variability, because the ocean–atmosphere coupling is strong, as it is likely to be in the Tropics. AMIP-type integrations also produce the right estimate for the atmospheric variability in the limit $\mu/\alpha \to 0$, because the ocean–atmosphere coupling becomes so weak that the SST variability has no effect on the atmosphere. However, for intermediate values for μ/α [i.e., $\mu/\alpha = O(1)$], which would be more characteristic of the extratropics, AMIP-type integrations would tend to underestimate the variability associated with the coupled system (see also Saravanan and McWilliams 1997).

To summarize, we have shown that a one-dimensional analytical stochastic model can lead to some important insights into the nature of ocean–atmosphere interaction, despite its extreme simplicity. The model envisages a scenario where spatially coherent and temporally incoherent atmospheric low-frequency variability plays a dominant role in forcing the ocean on decadal timescales. It shows how atmospheric spatial structures and oceanic advection can combine to produce preferred timescales of variability in certain parameter regimes. Such interactions could be responsible for the advective propagation of SST anomalies and the decadal timescales noted in observational studies (e.g., Sutton and Allan 1997). The analytical stochastic model also brings out the distinction between two types of oceanic feedback: the local thermodynamic feedback, and the nonlocal dynamic feedback.

Acknowledgments. We wish to thank M. Blackmon and Y.-H. Lee, for providing the CCM3 dataset, and F. Bryan, for providing the high-resolution CME model data. We wish to acknowledge discussions with G. Branstator, A. Capotondi, C. Deser, C. Penland, and P. Sardeshmukh that helped us better understand the stochastic aspects of climate variability. We also thank J. Tribbia for providing useful comments on the manuscript.

APPENDIX A

Discrete Fourier Transform of Covariances

The discrete equivalent of the Fourier transform as defined by (15) may be expressed as follows:

$$t_j = j\Delta t, \qquad j = 0, \ldots, N-1,$$

$$\nu_k = k\Delta\nu, \qquad k = -\frac{N}{2}, \ldots, \frac{N}{2} - 1,$$

$$\hat{f}_k \equiv \hat{f}(\nu_k) = \sum_j \Delta t e^{-i2\pi\nu_k t_j} f_j, \quad \text{and} \tag{A1}$$

$$f_j \equiv f(t_j) = \sum_k \Delta\nu e^{i2\pi\nu_k t_j} \hat{f}_k, \tag{A2}$$

where N is the number of data points in a time series, separated by sampling time interval Δt, and $\Delta\nu = (N\Delta t)^{-1}$ is the sampling frequency interval. The covariance $\mathrm{cov}(f, g; \tau_l)$ at lag $\tau_l = l\Delta t$ as given by (17) may be computed using a discrete Fourier transform as follows:

$$\mathrm{cov}(f, g; \tau_l) = \langle f_j g_{j+l} \rangle = \sum_k \Delta\nu e^{i2\pi\nu_k\tau_l} \sum_{k'} \Delta\nu e^{i2\pi t_j(\nu_k - \nu_{k'})} \langle \hat{f}^*_{k'} \hat{g}_k \rangle. \tag{A3}$$

The properties of discrete white-noise variables $A_f(t_n)$ and $B_f(t_n)$ may be written as

$$\langle \hat{A}^*_f(\nu_{k'}) \hat{A}_f(\nu_k) \rangle = \frac{\hat{a}^2}{\Delta\nu} \delta_{kk'}, \tag{A4}$$

$$\langle \hat{B}^*_f(\nu_{k'}) \hat{B}_f(\nu_k) \rangle = \frac{\hat{b}^2}{\Delta\nu} \delta_{kk'}. \tag{A5}$$

We typically choose $N = 8192$ and $\Delta t = 1/256$ when evaluating the discrete Fourier transforms.

Note that in the spatial domain, the covariance of the discrete white-noise variable $A_f(t_j)$ may be expressed as

$$\langle A_f(t_{j'}) A_f(t_j) \rangle = \frac{\hat{a}^2}{\Delta t} \delta_{jj'}, \tag{A6}$$

where the Δt factor takes into account the linear growth with time of the variance associated with a Wiener process.

APPENDIX B

Monopoles and Tripoles

In the above discussion, we have restricted ourselves to atmospheric forcing of the form $B_f \sin(2\pi y)$ in the domain $0 \le y \le 1$, that is, a dipole forcing [see (26)]. Since observed forcing patterns may have more, or less, structure than a dipole, we may ask how crucial is this choice for the operation of the advective resonance mechanism described above? To try to answer this question, we consider two other types of atmospheric forcing structures: (i) a monopole, that is, $B_f \sin(2\pi y)$, but only for $0 \le y \le 1/2$; (ii) a tripole, that is, $B_f \sin(2\pi y)$, but extended to $0 \le y \le 3/2$. We can simply use (25) to compute the response to the above two forcing structures, because the solution is valid over the whole domain $0 \le y < \infty$. Analogous to $\hat{B}_o$, we define the *direct* modes of oceanic response, $\hat{C}_o$ and $\hat{D}_o$, for the monopole and tripole forcing, respectively:

$$\hat{C}_o = 4 \int_0^{1/2} dy\, \hat{T}_o(y) \sin 2\pi y$$

$$\hat{D}_o = \frac{4}{3} \int_0^{3/2} dy\, \hat{T}_o(y) \sin 2\pi y. \tag{B1}$$

Figure B1 shows the frequency-variance spectra $\langle |\hat{B}_o(\nu)|^2 \rangle$, $\langle |\hat{C}_o(\nu)|^2 \rangle$, and $\langle |\hat{D}_o(\nu)|^2 \rangle$ for $\Gamma = 4$. We see that for monopole forcing, there is no preferred frequency. For tripole forcing, the peak near $\nu = 1$

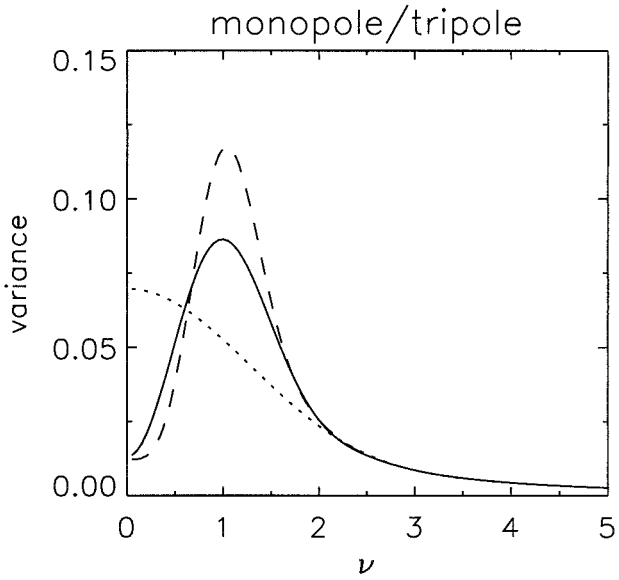

FIG. B1. Frequency spectrum of oceanic temperature variance associated with the direct mode of response for $\Gamma = 4$: monopole (dotted), dipole (solid), and tripole (dashed) forcing profiles.

is stronger and sharper as compared to dipole forcing. Note that for tripole forcing, the spectral peak still occurs at $\nu \approx 1$, although the y domain has been extended from (0, 1) to (0, 1.5). This means that it is the ''wavelength'' of the forcing, not the domain size, that determines the length scale of interest. The spectra for $\Gamma = 16$ (not shown) are also qualitatively similar. In other words, the sharpness of the peak in the wavenumber-variance spectrum of the atmospheric forcing is reflected in the sharpness of the peak in the frequency-variance spectrum of the oceanic response in the fast–deep regime. Thus, having more ''poles'' in the forcing structure strengthens the ''advective resonance'' effect, with a dipole being the minimum requirement.

APPENDIX C

Phase Relationships

If we take the stochastic atmospheric forcing term $\hat{B}_f$ in (20) to have 0 phase (i.e., a real number), then the phase of the direct and orthogonal modes of oceanic response would be given by $\arctan(\mathrm{Im}\hat{B}_o/\mathrm{Re}\hat{B}_o)$ and $\arctan(\mathrm{Im}\hat{A}_o/\mathrm{Re}\hat{A}_o)$, respectively. This phase relationship is shown as a function of ν in Fig. C1. In the slow–shallow regime, the direct mode tends to be approximately in phase with the forcing, with a slight lag, for $\nu \approx 1$. In the fast–deep regime, the direct mode appears to ''lead'' the forcing slightly for $\nu < 1$. However, the lag correlations (discussed below) clearly show that the forcing always leads the response. Therefore, the lead in the phase of the response is a cautionary example about inferring causality from spectral phases. For $\nu > 2$, the direct mode of response is in quadrature with the forcing. The phase of the orthogonal mode in the slow–shallow regime is irrelevant because of its very weak amplitude. In the fast–deep regime, the orthogonal mode is in phase with the forcing for $\nu > 2$. That is, the orthogonal mode is in temporal quadrature with the direct mode.

Using (17), (18), and (29), we compute the covariance between the modes of oceanic response and white-noise atmospheric forcing, $\mathrm{cov}(\hat{B}_f, \hat{B}_o; \tau)$, and $\mathrm{cov}(\hat{B}_f, \hat{A}_o; \tau)$. The covariances are computed analytically by inverting the Fourier transform through contour integration in the complex ν plane, where the poles are located at $\nu = \pm 1 + i/\Gamma$. The only subtlety being that, because of the complex exponential terms, the contour needs to be closed differently for the various terms in the integrand for different regimes of τ values. The resulting expressions for the covariances are

$$c_{BB}(\tau) \equiv \mathrm{cov}(\hat{B}_f, \hat{B}_o; \tau) = \begin{cases} \hat{b}^2 \dfrac{1}{\Gamma} e^{-2\pi\tau/\Gamma}\{(1-\tau)2\pi \cos 2\pi\tau + \sin 2\pi\tau\}, & \text{for } 0 \le \tau \le 1, \\ 0, & \text{otherwise;} \end{cases}$$

$$c_{BA}(\tau) \equiv \mathrm{cov}(\hat{B}_f, \hat{A}_o; \tau) = \begin{cases} -\hat{b}^2 \dfrac{1}{\Gamma} e^{-2\pi\tau/\Gamma}\{(1-\tau)2\pi \sin 2\pi\tau\}, & \text{for } 0 \le \tau \le 1, \\ 0, & \text{otherwise,} \end{cases} \tag{C1}$$

where positive τ implies that the oceanic response lags the atmospheric forcing.

Interestingly, the covariances c_{BB} and c_{BA} vanish identically not just for $\tau < 0$, as would be the case with a red-noise model, but also for $\tau > 1$. This should not be surprising, because all the information in the model domain $0 \le y \le 1$ is advected out of it for $\tau > 1$. Although the covariances given by (C1) can be used to compute the actual correlation coefficient, that would involve having to specify the total amount of

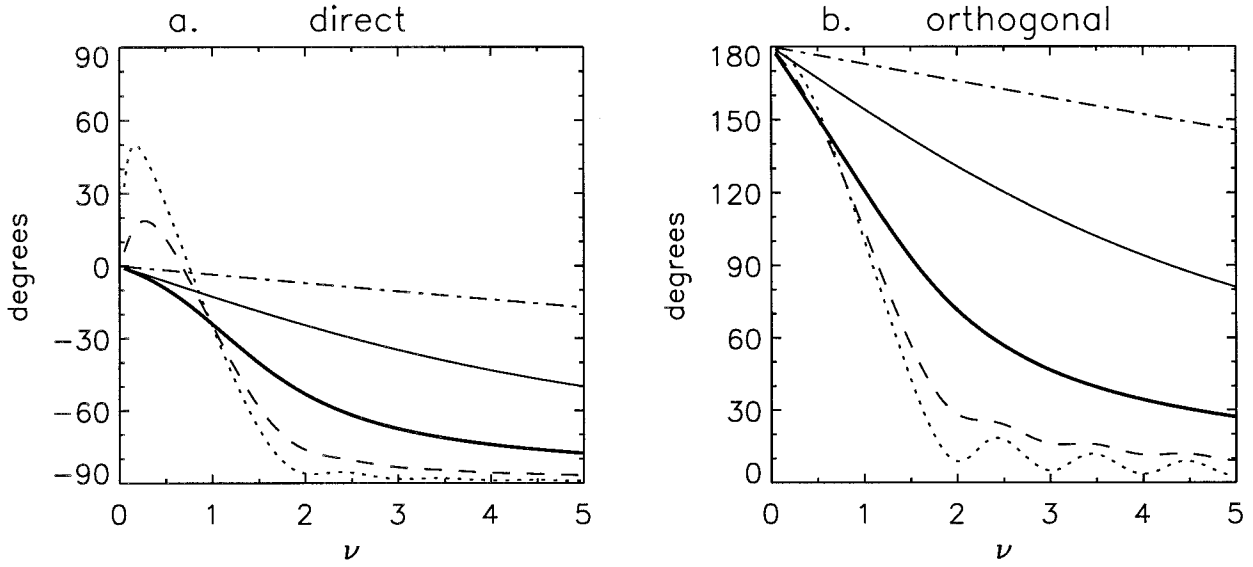

FIG. C1. Phase of the oceanic temperature response (in degrees), with respect to the atmospheric forcing, for $\Gamma = 1/16, 1/4, 1, 4, 16$: (a) direct mode ($\hat{B}_o$); (b) orthogonal mode ($\hat{A}_o$). Positive phase implies that the ocean leads the atmosphere. (Lines as in Fig. 7.)

variance associated with the ''white-noise'' forcing. Instead, we consider the normalized covariance, for example, $c_{BB}/\max(|c_{BB}|)$, where the covariance is normalized by its maximum absolute value. This would be proportional to the correlation coefficient. For direct mode of response, the normalized covariance has a maximum at $\tau = 0$ (Fig. C2a). In the slow–shallow regime, the covariance essentially decays exponentially for $\tau > 0$, in a manner very similar to a red-noise response. In the fast–deep regime, the covariance shows nonmonotonic behavior with a negative minimum at $\tau \approx 0.5$. For the orthogonal mode of response, the covariance vanishes at $\tau = 0$ (Fig. C2b). In the slow–shallow regime, the covariance exhibits a strong minimum fairly close to $\tau = 0$ and then decays very rapidly. In the fast–deep regime, the minimum covariance occurs at $\tau \approx 0.2$, followed by a weaker maximum at $\tau \approx 0.7$.

Also of interest is the autocorrelation of the modes of oceanic response, $\mathrm{cov}(\hat{B}_o, \hat{B}_o; \tau)$, and $\mathrm{cov}(\hat{A}_o, \hat{A}_o; \tau)$ (not shown). The autocorrelations show features similar to that seen in the covariances. In the slow–

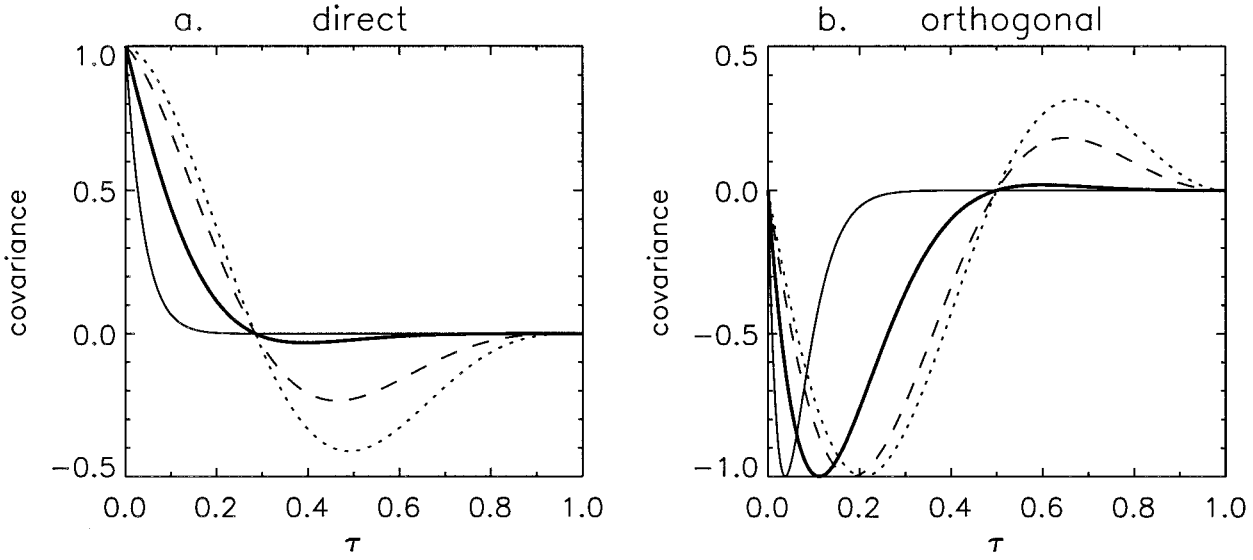

FIG. C2. Normalized covariance between the oceanic temperature response and the atmospheric forcing, as a function of lag τ, for $\Gamma = 1/16, 1/4, 1, 4, 16$: (a) direct mode (normalized c_{BB}); (b) orthogonal mode (normalized c_{BA}). Positive τ implies that the ocean lags the atmosphere. (Lines as in Fig. 7.)

shallow regime, the autocorrelation shows exponential decay away from the peak at $\tau = 0$. In the fast–deep regime, the autocorrelation decays nonmonotonically, with negative minima around $\tau \approx 0.4$.

To summarize, the autocorrelation of the modes of oceanic response, and their covariance with the atmospheric forcing, reflect the structure of the frequency spectra shown in Fig. 11. In the slow–shallow regime, there is no peak in the frequency spectrum, and the covariance and the autocorrelation show rednoise type of behavior. In the fast–deep regime, there is a peak in the frequency spectrum near $\nu = 1$, and a corresponding negative minimum at $\tau = 0.4$–0.5 in the covariance and the autocorrelation.

REFERENCES

Barsugli, J. J., and D. S. Battisti, 1998: The basic effects of atmosphere–ocean thermal coupling on midlatitude variability. *J. Atmos. Sci.,* **55,** 477–493.

Battisti, D. S., U. S. Bhatt, and M. A. Alexander, 1995: A modeling study of interannual variability in the wintertime North Atlantic Ocean. *J. Climate,* **8,** 3067–3083.

Borges, M. D., and P. D. Sardeshmukh, 1995: Barotropic Rossby wave dynamics of zonally varying upper-level flows during northern winter. *J. Atmos. Sci.,* **52,** 3780–3796.

Branstator, G., 1992: The maintenance of low-frequency atmospheric anomalies. *J. Atmos. Sci.,* **49,** 1924–1945.

——, A. Mai, and D. Baumhefner, 1993: Identification of highly predictable flow elements for spatial filtering of medium- and extended-range numerical forecasts. *Mon. Wea. Rev.,* **121,** 1786–1802.

Bryan, F. O., C. W. Boning, and W. R. Holland, 1995: On the midlatitude circulation in a high resolution model of the North Atlantic. *J. Phys. Oceanogr.,* **25,** 289–305.

Capotondi, A., and W. R. Holland, 1997: Decadal variability in an idealized ocean model and its sensitivity to surface boundary conditions. *J. Phys. Oceanogr.,* **27,** 1072–1093.

Davis, R. E., 1976: Predictability of sea surface temperature anomalies and sea level pressure anomalies over the North Pacific ocean. *J. Phys. Oceanogr.,* **6,** 249–266.

Delworth, T., 1996: North Atlantic interannual variability in a coupled ocean–atmosphere model. *J. Climate,* **9,** 2356–2375.

——, S. Manabe, and R. J. Stouffer, 1993: Interdecadal variations of the thermohaline circulation in a coupled ocean–atmosphere model. *J. Climate,* **6,** 1993–2011.

Dennery, P., and A. Krzywicki, 1967: *Mathematics for Physicists.* Harper and Row, 384 pp.

Deser, C., and M. L. Blackmon, 1993: Surface climate variations over the North Atlantic ocean during winter: 1900–1989. *J. Climate,* **6,** 1743–1753.

——, M. A. Alexander, and M. S. Timlin, 1996: Upper ocean thermal variations in the North Pacific during 1970–1991. *J. Climate,* **9,** 1840–1855.

Feldstein, S. B., and W. A. Robinson, 1994: Comments on 'Spatial structure of ultra-low frequency variability in a simple atmospheric circulation model.' *Quart. J. Roy. Meteor. Soc.,* **120,** 739–745.

Frankignoul, C., 1985: Sea surface temperature anomalies, planetary waves, and air–sea feedback in the middle latitudes. *Rev. Geophys.,* **23,** 357–390.

——, and K. Hasselmann, 1977: Stochastic climate models: Part I. Application to sea surface temperature anomalies and thermocline variability. *Tellus,* **29,** 289–305.

——, and R. W. Reynolds, 1983: Testing a dynamical model for mid-latitude sea surface temperature anomalies. *J. Phys. Oceanogr.,* **13,** 1131–1145.

Griffies, S. M., and E. Tziperman, 1995: A linear thermohaline oscillator driven by stochastic atmospheric forcing. *J. Climate,* **8,** 2440–2453.

Hasselmann, K., 1976: Stochastic climate models: Part I. Theory. *Tellus,* **28,** 473–485.

Haney, R. L., 1971: Surface thermal boundary condition for ocean circulation models. *J. Phys. Oceanogr.,* **1,** 241–248.

Held, I. M., 1983: Stationary and quasi-stationary eddies in the extratropical troposphere: A theory. *Large-Scale Dynamical Processes in the Atmosphere,* B. J. Hoskins and R. Pearce, Eds., Academic Press, 127–168.

Herterich, K., and K. Hasselmann, 1987: Extraction of mixed layer advection velocities, diffusion coefficients, feedback factors, and atmospheric forcing parameters from the statistical analysis of North Pacific SST anomaly fields. *J. Phys. Oceanogr.,* **17,** 2145–2156.

Hoerling, M. P., M. Ting, and A. Kumar, 1995: Zonal flow-stationary wave relationship during El Niño: Implications for seasonal forecasting. *J. Climate,* **8,** 1838–1852.

Kiehl, J. T., J. J. Hack, G. B. Bonan, B. A. Boville, B. P. Briegleb, D. L. Williamson, and P. J. Rasch, 1996: Description of the NCAR Community Climate Model (CCM3). NCAR Tech. Note NCAR / TN-420+STR, 152 pp. [Available from the National Center for Atmospheric Research, P.O. Box 3000, Boulder, CO 80307.]

Kushnir, Y., 1994: Interdecadal variations in North Atlantic sea surface temperature and associated atmospheric conditions. *J. Climate,* **7,** 141–157.

Large, W. G., G. Danabasoglu, S. C. Doney, and J. C. McWilliams, 1997: Sensitivity to surface forcing and boundary layer mixing in the NCAR CSM ocean model. *J. Phys. Oceanogr.,* **27,** 2418–2447.

Latif, M., and T. P. Barnett, 1994: Causes of decadal climate variability over the North Pacific and North America. *Science,* **266,** 634–637.

Lau, N.-C., and M. J. Nath, 1994: A modeling study of the relative roles of tropical and extratropical SST anomalies in the variability of the global atmosphere–ocean system. *J. Climate,* **7,** 1184–1207.

Lemke, P., E. W. Trinkl, and K. Hasselmann, 1980: Stochastic dynamic analysis of polar sea-ice variability. *J. Phys. Oceanogr.,* **10,** 2100–2120.

Levitus, S., J. I. Antonov, and T. P. Boyer, 1994: Interannual variability of temperature at a depth of 125 meters in the North Atlantic Ocean. *Science,* **266,** 96–99.

Lorenz, E. N., 1973: On the existence of extended range predictability. *J. Appl. Meteor.,* **12,** 543–546.

Marotzke, J., and D. W. Pierce, 1997: On spatial scales and lifetimes of SST anomalies beneath a diffusive atmosphere. *J. Phys. Oceanogr.,* **27,** 133–139.

Mikolajewicz, U., and E. Maier-Reimer, 1990: Internal secular variability in an ocean general circulation model. *Climate Dyn.,* **4,** 145–156.

Mysak, L. A., T. F. Stocker, and F. Huang, 1993: Century-scale variability in a randomly forced two-dimensional thermohaline ocean model. *Climate Dyn.,* **8,** 103–116.

Nitsche, G., and J. M. Wallace, 1995: Interannual and intraseasonal variability in a fixed SST, perpetual January GCM run. *Proc. Sixth Int. Meeting on Statistical Climatology,* Galway, Ireland, 521–524.

Penland, C., and L. Matrosova, 1994: A balance condition for stochastic numerical models with application to the El Niño–Southern Oscillation. *J. Climate,* **7,** 1352–1372.

Rahmstorf, S., and J. Willebrand, 1995: The role of temperature feedback in stabilizing the thermohaline circulation. *J. Phys. Oceanogr.,* **25,** 788–805.

Rayner, N. A., C. K. Folland, D. E. Parker, and E. B. Horton, 1995: A new global sea-ice and sea surface temperature (GISST) data set for 1903–1994 for forcing climate models. Hadley Centre Internal Note 69, 9 pp. [Available from the

Hadley Centre, Meteorological Office, Bracknell, Berkshire RG12 2SY, United Kingdom.]

Saravanan, R., 1998: Atmospheric low-frequency variability and its relationship to midlatitude SST variability: Studies using the NCAR Climate System Model. *J. Climate*, in press.

——, and J. C. McWilliams, 1995: Multiple equilibria, natural variability, and climate transitions in an idealized ocean–atmosphere model. *J. Climate*, **8,** 2296–2323.

——, and ——, 1997: Stochasticity and spatial resonance in interdecadal climate fluctuations. *J. Climate*, **10,** 2299–2320.

Sutton, R. T., and M. R. Allen, 1997: Decadal predictability of North Atlantic sea surface temperature and climate. *Nature*, **388,** 563–565.

Voorhis, A. D., E. H. Schroeder, and A. Leetma, 1976: The influence of deep mesoscale eddies on sea surface temperature in North Atlantic subtropical convergence. *J. Phys. Oceanogr.*, **6,** 953–961.

Wallace, J. M., and D. S. Gutzler, 1981: Teleconnections in the geopotential height field during the Northern Hemisphere winter. *Mon. Wea. Rev.*, **109,** 784–812.

Weaver, A. J., and E. S. Sarachik, 1991: Evidence for decadal variability in an ocean general circulation model: An advective mechanism. *Atmos.–Ocean*, **29,** 197–231.

——, ——, and J. Marotzke, 1991: Freshwater flux forcing of decadal and interdecadal variability. *Nature*, **353,** 836–838.

Weisse, R., U. Mikolajewicz, and E. Maier-Reimer, 1994: Decadal atmosphere–ocean variations in the Pacific. *J. Geophys. Res.*, **99,** 12 411–12 421.

Welander, P., 1985: Thermohaline effects in the ocean circulation and related simple models. *Large-Scale Transport Processes in the Oceans and the Atmosphere*, D. L. T. Anderson and J. Willebrand, Eds., NATO ASI Series, Reidel, 163–223.

Winton, M., and E. S. Sarachik, 1993: Thermohaline oscillations induced by strong steady salinity forcing of ocean general circulation models. *J. Phys. Oceanogr.*, **23,** 1389–1410.